www.sciencemag.org/cgi/content/full/science.1203513/DC1

Supporting Online Material for

Climate Sensitivity Estimated from Temperature Reconstructions of the Last Glacial Maximum

Andreas Schmittner,* Nathan M. Urban, Jeremy D. Shakun, Natalie M. Mahowald, Peter U. Clark, Patrick J. Bartlein, Alan C. Mix, Antoni Rosell-Melé

*To whom correspondence should be addressed. E-mail: aschmitt@coas.oregonstate.edu

Published 24 November 2011 on *Science* Express
DOI: 10.1126/science.1203513

This PDF file includes:

Supporting Online Material to

"Climate Sensitivity Estimated From Temperature Reconstructions of the Last Glacial Maximum" by Schmittner, A., N. M. Urban, J. D. Shakun, N. D. Mahowald, P. U. Clark, P. J. Bartlein, A. C. Mix, and A. Rosell-Melé (2011) Science

Contents:

1. Climate Model, Radiative Forcing and Ensemble Generation

The UVic Earth System Climate Model (version 2.8 with parameters as described in detail in (*28*)) includes a three-dimensional ocean general circulation model, a dynamic-thermodynamic sea ice model, a simple one-layer energy-moisture balance model of the atmosphere as well as land-surface and dynamic terrestrial vegetation components at a resolution of 1.8°×3.6° with 19 vertical levels in the ocean. Since vegetation is allowed to respond dynamically to changes in climate and CO_2 concentrations, it is treated as an internal interactive feedback, rather than as part of the prescribed forcing as in previous studies without interactive vegetation.

In order to generate model versions with different climate sensitivities we have changed a parameter in the formulation of outgoing planetary longwave radiation at the top-of-the-atmosphere Q_{PLW} in the atmospheric Energy-Moisture Balance Model (EMBM) of the UVic model version 2.8 (*14, 28*). The UVic model uses a polynomial formulation by Thompson and Warren (*29*):

$$Q_{PLW} = c_{00} + c_{01}r + c_{02}r^2 + (c_{10} + c_{11}r + c_{12}r^2)T_a + (c_{20} + c_{21}r + c_{22}r^2)T_a^2 + (c_{30} + c_{31}r + c_{32}r^2)T_a^3 \quad \text{(S1)}$$

that depends on surface air temperature T_a and surface relative humidity r. In order to keep global preindustrial surface air temperature constant we varied the slope of this curve with respect to T_a by changing c_{10} and c_{00} simultaneously (Figure S1). Equation S1 implicitly includes the effects of the water vapor and lapse-rate feedbacks as well as cloud feedbacks on infrared radiation. The larger the slope c_{10} the larger the response of Q_{PLW} will be to a given change in temperature. Since this is a negative feedback, the climate sensitivity is smaller the larger the slope c_{10}. We have created an ensemble of 25 different model versions by varying c_{10} from 1.7 to 18.1 $Wm^{-2}K^{-1}$. The standard model uses c_{10} = 2.6 $Wm^{-2}K^{-1}$. Present-day observations do not provide firm constraints on these

parameters as illustrated in Figure S1, although very small and very large values can probably be excluded. However, we have retained models with extreme values in order to gauge the constraints imposed by LGM data only, without considering constraints from present day observations.

We carried out three types of simulations with each ensemble member: a pre-industrial control run, a double CO_2 run (to determine ECS_{2xC}) and four LGM experiments. The LGM experiments consider uncertainty in dust forcing, wind stress and initial conditions (different initial states of the Atlantic Meridional Overturning Circulation AMOC). All simulations were integrated for 2000 years after which surface climate is close to equilibrium. (E.g. global mean surface air temperature changes by 2.2×10^{-4} K/yr for ECS_{2xC}=5.6). The average of the last 500 years were used for the analysis.

Our standard model simulations of the Last Glacial Maximum (LGM) include radiative forcing from larger continental ice sheets (ΔF_{sfc} = –2.2 W/m^2) (*30*), lower greenhouse gas concentrations (CO_2, CH_4, N_2O) ($\Delta F_{GHG} = \Delta F_{CO2} + \Delta F_{CH4} + \Delta F_{N2O}$ = –2.8 W/m^2) (*31-33*), changes in the seasonal distribution of insolation (annually averaged ΔF_{ins} = 0 W/m^2), and higher atmospheric dust levels (Figure S2; ΔF_{dust} = –0.9 W/m^2) (*34*). The total radiative forcing in the standard model $\Delta F_{LGM} = \Delta F_{sfc} + \Delta F_{GHG} + \Delta F_{dust}$ = –5.9 W/m^2 is similar to previous estimates (*35*), but less than another recent study (*36*) who estimated ΔF_{LGM} = –9.5 W/m^2, partly because of higher assumed dust ΔF_{dust} = –1.9 W/m^2 and ice sheet ΔF_{sfc} = –3.2 W/m^2 forcing by Köhler et al. and because they prescribe surface albedo changed from changes in vegetation ΔF_{veg} = –1.1 W/m^2, which is considered an internal feedback in our study.

Twenty-two additional LGM experiments have been conducted with varying dust forcing and surface wind stress anomalies, but our ensemble does not explore uncertainties in surface or greenhouse gas forcings.

Ice sheets are prescribed as fixed differences in the surface elevation in the model (not interactive). This affects surface air temperatures according to a fixed lapse rate (5K/km), which leads to a changed albedo because of accumulating snow cover. (Albedo is not prescribed.) Forcing due to surface albedo changes associated with the increased land area covered with ice sheets was estimated by performing an additional simulation with pre-industrial boundary conditions but added LGM ice sheets. The difference in shortwave fluxes at the top of the atmosphere between this experiment and the pre-industrial control run gives the forcing due to surface albedo changes resulting in the value of ΔF_{sfc} = –2.2 W/m^2 reported above. Northern hemisphere ice sheets contribute –1.8 W/m^2, southern hemisphere ice sheets –0.3 W/m^2 and changes in non-ice sheet covered areas –0.1 W/m^2. This estimate, which includes the effects of changes in snow cover, is within the range (–1.9 to –2.9 W/m^2) of previous studies (*37-40*) but smaller than the –3.2 W/m^2 by *Köhler et al.* (*36*). We do not consider the effect of surface albedo changes caused by differences in land-sea distribution away from ice sheets associated with exposed continental shelves. This effect has been estimated to be small (–0.4 W/m^2) (*38*). Including this forcing, which is 7% of the total, could decrease our estimate of ECS_{2xC} slightly (by up to 0.2 K).

For dust we use two-dimensional maps (Figure S2) of longwave and shortwave

radiative forcing for the LGM and pre-industrial climate as simulated by the interactive dust model of (*34*), which uses the Community Atmospheric Model, as described in (*11*). The dust model results were tuned for the LGM to best match available deposition observations, and matched these observations for the current climate, especially in the annual mean. The shortwave and longwave impacts of desert dust were included, as described in (*41*). We assumed the best available optical values for the desert dust particles (*41*), but these are uncertain (*42*), and there are large differences in the results if different optical values are used (*43*).

2. Temperature Reconstructions

We have combined recent syntheses of global sea surface temperatures (SSTs) from the Multiproxy Approach for the Reconstruction of the Glacial Ocean (MARGO) project (*12*) and surface air temperatures (SAT) over land based on pollen distributions (*13*), with additional data (see subsection 2.1 below) from ice sheets, land and ocean (*44*). The combined temperature reconstructions are shown in Figure 1. The published error estimates are shown in Figure S3.

2.1. Shakun et al. (2011) LGM temperature dataset

This dataset (Table 1) consists of 54 proxy temperature records spanning some or the entire LGM interval (19-23 ka) that are not included in the MARGO (2009) or Bartlein et al. (2011) datasets. The records are based on various proxies from ocean, land, and ice, including alkenones (n=21), foraminiferal Mg/Ca (n=18), foraminiferal assemblages (n=4), TEX_{86} (n=4), MBT/CBT (n=2), and ice cores (n=5). LGM temperature anomalies and errors were calculated following the methods used by MARGO (2009). One difference, however, is that many of these records (n=34) are high-resolution time series that extend to the late Holocene. Therefore, LGM anomalies for these records were calculated as the difference between the 19-23 ka and 0-2 ka means. This approach only assumes that the proxies accurately record the magnitude of LGM-Late Holocene temperature change, rather than absolute LGM temperatures. For the remaining 20 records, LGM anomalies were calculated from modern mean annual temperature at 10 m water depth using the World Ocean Atlas 98 dataset, as done by MARGO (2009). Twenty-six of the ocean records come from locations where the MARGO 5°x5° LGM temperature anomaly grid already contains values. Therefore, these MARGO grid points were updated with these new records, and errors were propagated following MARGO's (2009) methods. The dataset is available at http://mgg.coas.oregonstate.edu/~andreas/data/schmittner11sci/.

2.2 Mg/Ca salinity bias

Recent research suggests that foraminiferal Mg/Ca may be sensitive to salinity (*45, 46*). If so, correcting Mg/Ca records for the ~1 unit increase in global ocean salinity at the LGM would decrease reconstructed SSTs. The magnitude of this temperature correction would vary with the absolute value of the salinity and SST at the core site due to the nonlinear relationships between salinity and "excess Mg/Ca", and Mg/Ca and SST. For example, (*46*) estimate an additional 1°C LGM cooling for a western tropical Pacific record, while (*45*) calculate an additional 1.8°C cooling for a Caribbean record. Since none of the Mg/Ca records used in our study have been corrected for this salinity effect, taking it into account would increase reconstructed LGM cooling and thus our estimate of

climate sensitivity. Nonetheless, we estimate that the impact on our results would be minor. In particular, Mg/Ca accounts for only 9% (66 of 742) of the individual SST reconstructions used here, and only 5% of the global (ocean and land) temperature reconstructions. Moreover, it is unclear now many of these Mg/Ca reconstructions were affected by large salinity changes that would introduce a bias since it only occurs at high salinities (>35) (*45*). Assuming a typical temperature correction of -1°C for all Mg/Ca records due to this salinity effect and averaging that through to the LGM global cooling estimate would increase it on the order of ~0.05°C (i.e., 5% of 1°C). This is well within the error of our 3.6 ± 1°C LGM cooling estimate and would have little effect on the likely range of climate sensitivity we report.

The reconstructed LGM-modern temperature anomalies are plotted against the reconstruction errors in Figure S4. Land points show greater LGM cooling than ocean points. The SST proxies, however, generally have greater reconstruction errors than the land proxies.

3. Snowball Earth

Figure S5 shows three snapshots in the transition to a completely ice covered Earth for a high climate sensitivity model (ECS_{2xC} = 8.2 K). Shortly after model year 460, that is 460 years after the switch to LGM boundary conditions, Earth is completely ice covered in this simulation.

4. Simulated Ocean Circulation

For LGM boundary conditions the standard model exhibits a threshold around ECS_{2xC}=2.7 at which the Meridional Overturning Circulation (MOC) of the ocean changes from a mode with deep water formation in the North Atlantic (ECS_{2xC}<2.7) to a mode with deep water formation in the North Pacific (ECS_{2xC}>2.7) as illustrated in Figure S6. Note that only an index of the Atlantic MOC is shown in Figure S6, but inspection of the full streamfunction shows that the mode with zero AMOC exhibits sinking in the North Pacific down to about 2000 m depth (not shown) due to the Atlantic-Pacific seesaw mechanism (*47*), whereas the mode with active AMOC has no deep water formation in the North Pacific. The mode with deep water formation in the North Atlantic is consistent with the observed modern circulation pattern whereas the mode with sinking in the North Pacific is not. Paleoclimate data show that deep water formation in the North Atlantic was active during the LGM (albeit perhaps weaker and/or shallower than at present day) (*48*) contrary to the standard model results for high climate sensitivities. Sensitivity experiments with added wind stress anomalies from a coupled ocean-atmosphere model (GENMOM) (*49*) result in a stronger AMOC than that of the control simulation and do not exhibit the threshold seen in the model without wind stress anomalies. Results from these experiments show that the climate sensitivity estimates do not depend much on the state of the MOC (subsection 7.3).

5. Data-Model Comparisons and Residual Analysis

Figure S7 shows the zonally averaged temperature changes from the best fitting model (ECS_{2xC}=2.4 K), Figure S8 shows the spatial distribution of the residuals (model minus reconstructions). The correlation coefficient for the 2D temperature changes is 0.53 and the root mean squared error is 2.3 K.

Histograms of reconstructed temperature anomalies are plotted against the modeled temperature anomalies for several different climate sensitivites in Figure S9. The reconstructed SSTs are most compatible with a model ECS_{2xC} near 2 K, whereas the reconstructed land SATs are most compatible with a model ECS_{2xC} near 3 or 4 K, when comparing peaks of the reconstructed and modeled anomaly distributions. When land and ocean anomalies are considered together, an ECS_{2xC} near 2 K is favored when comparing peaks, similar to the SST comparison, likely because the ocean data are more abundant than the land data.

The data-model residual temperature anomalies are plotted in Figure S10 for ECS_{2xC} = 2.2 K. The residuals show some evidence of non-normality. However, the land and ocean residuals individually appear more normal, suggesting that the combined residuals are a mixture of two normal distributions. This motivates a statistical treatment of the data as normally distributed with different covariance structures over land and ocean. The land residuals show greater variability than the ocean residuals, as might be expected. Neither the land nor ocean residuals display a strong skewness, nor particularly heavy tails. While the ocean residuals are centered at zero the land residuals are not, indicating that the land data do not favor this ECS_{2xC} value.

To further explore the differences between the ECS_{2xC} values implied by the land and ocean data, Figure S11 plots the mean and 90% interval of the reconstructed temperature anomalies against the mean and 90% interval of the modeled temperature anomalies as a function of model ECS_{2xC}. The range of modeled land SAT anomalies lies within the range of reconstructed SAT anomalies for ECS_{2xC} below ~5 K, whereas the range of modeled ocean SST anomalies lies within the range of reconstructed SST anomalies for ECS_{2xC} below ~3 K. This is compatible with the Figure S9, which shows that the ocean SST data favor lower ECS_{2xC} values than the land SAT data.

The modeled ocean anomalies also show an abrupt decrease in the lower temperature range near ECS_{2xC} = 2.7 K, where the AMOC collapses (Fig. S6). Figure S12 shows a data model comparison with the North Atlantic points excluded. (The excluded region is defined empirically to be those Northern Hemisphere ocean grid cells for which the modeled temperature anomaly in the ECS_{2xC} = 2.83 K run is more than 1 K colder than the anomalies in the ECS_{2xC} = 2.51 K run. This includes most of the North Atlantic and Mediterranean Sea, and no other grid cells.) The data-model comparison suggests that SST data outside of the North Atlantic region are compatible with a larger range of climate sensitivities (below ECS_{2xC} = 4 K) than are the SST data with the AMOC region included (as discussed above).

6. Statistical Analysis

6.1 Regridding and Sea Level Correction

For the purpose of data-model comparison the model output is mapped from the UVic grid (1.8×3.6°) onto the grids of the temperature reconstructions (5×5° grid for the SSTs and Shakun et al. data and 2×2° grid for the pollen data). A correction of 0.32 K is added to the modeled SST everywhere in order to account for the 120 m lower sea level at the LGM. The value of ΔSST_{SL} = 0.32 K is determined from an additional model simulation in which sea level is explicitly lowered and a constant global mean lapse rate of 5 K km^{-1} is used to calculate surface air temperatures. The analysis uses modeled SSTs over the

oceans and SATs over land.

6.2 Model Emulation

In order to predict the model output at arbitrary climate sensitivities, the model output at each grid cell is emulated by linear interpolation of the model output over the ECS_{2xC} values in the ensemble. A total of n=435 independent linear emulators are constructed, one for each grid cell containing data. In addition to a linear interpolator, several other types of statistical emulators were also evaluated, including independent cubic spline interpolators, independent thin-plate spline interpolators, and a Gaussian process outer product emulator with a linear mean function and an exponential covariance function separable in latitude and longitude. None produce obviously better emulation than the simple linear emulator, and most suffer from some 'overshoot' problems where the emulator failed to capture rapid changes in output near ECS_{2xC} = 2.7 K, at which the AMOC collapses (Figure S6). A linear interpolator emulator has the disadvantage of not being able to estimate its own interpolation uncertainty ('code uncertainty'), but the code uncertainty estimates from the Gaussian process emulator were much smaller than the temperature reconstruction and UVic model errors, and are presumably negligible in the inference.

6.3 Statistical Model

For statistical analysis it is assumed that the temperature anomaly reconstructions are normally distributed about the (emulated) modeled anomalies for some "best" value of ECS_{2xC}, possibly with some bias (b). That is,

$$T_{obs} \sim \mathrm{N}(\mu = T_{mod}(ECS_{2xC}) + b, \Sigma) , \qquad \text{(S2)}$$

or, equivalently,

$$T_{obs} = T_{mod}(ECS_{2xC}) + b + \varepsilon, \ \varepsilon \sim \mathrm{N}(\mu = 0, \Sigma) \qquad \text{(S3)}$$

where T_{obs}, T_{mod}, b, and ε are vectors of length n, and Σ is an $n \times n$ covariance matrix describing the model and observation errors. The inference problem is to compute a probability density function for ECS_{2xC} conditional on the observations, $p(ECS_{2xC} | T_{obs})$.

To account for the possibility of different biases and errors over land and ocean (see Residual Analysis), the vectors and matrices are decomposed into separate land and ocean blocks. The bias is then $b = [b_L \ b_O]$ where b_L and b_O are constant vectors of length n_L = 113 and n_O = 322. (Here and elsewhere the same symbol is used to refer to both a scalar and a constant vector equal elementwise to that scalar.) Conceptually a bias can be attributed to systematic errors in the modeled temperatures, the proxy temperature reconstructions, or both. While the UVic model does have spatial biases in surface temperature, the bias in the LGM-modern temperature anomaly should be reduced if the model makes similar absolute errors in the LGM and modern periods. The reconstructions may contain biases e.g. due to age model errors. Since the LGM corresponds to a temperature minimum in time in most regions age model errors can lead to systematically warmer reconstructions. In the default analysis the bias is assumed to be zero, because it is highly confounded with climate sensitivity, the quantity of interest. Arbitrarily large climate sensitivities (cold LGM temperature anomalies) can be made compatible with the data by introducing a sufficiently large positive model bias, and similarly for arbitrarily small climate sensitivities. We later consider sensitivity tests in

which small nonzero biases over land or ocean are assumed.

The error covariance matrix is decomposed into the sum of three different sources of error: observation (proxy) error, spatially correlated error, and an additional small-scale, spatially independent source of error referred to in geostatistics as a 'nugget':

$$\Sigma = \Sigma_{obs} + \Sigma_{spatial} + \Sigma_{nugget} . \quad \text{(S4)}$$

The proxy reconstruction errors form a vector σ_{obs}. Assuming the reconstruction errors are spatially independent, the corresponding covariance matrix is diagonal containing the error variances, $\Sigma_{obs} = \mathrm{diag}(\sigma_{obs}^2)$. The reconstruction errors are likely not completely spatially independent, but the proxy error estimates used in this analysis do not include estimates of spatial correlation. With sufficient data and a perfect model it is possible to estimate the spatial correlation from the data-model residuals. However, the model is not perfect and its errors are also spatially correlated. Without knowing the reconstruction or model error *a priori*, there is confounding between the two sources of error and their spatial structures cannot be estimated independently.

The other two error terms (spatial and nugget) are introduced to account for this confounding between observation and model error. The spatial error term represents all the spatial dependence in the total residual errors, including both reconstruction and model spatial error. The spatial correlation function is assumed to be exponentially decaying in distance,

$$\mathrm{cor}(x_i, x_j) = \exp[-d(x_i, x_j)/\lambda] , \quad \text{(S5)}$$

where the function $d(\cdot,\cdot)$ gives the geodesic distance between two points on the Earth's surface, and $\lambda = 2000$ km is a spatial correlation *e*-folding length scale. Future work could make use of more sophisticated (albeit computationally expensive) approaches for specifying covariance functions on the sphere (*50*).

This correlation function is homogeneous and isotropic, assigning the same correlation length scale over land and ocean, and in zonal and meridional directions. These assumptions are only approximately correct; for example, one might expect the correlation length to be longer over ocean than land, or longer within a latitudinal zone than along a longitudinal meridian. The latter expectation could be addressed with a correlation function that is separable in latitude and longitude, with separate correlation lengths for each, but it its unclear how then to properly account for geodesic distances on the sphere while maintaining zonal/meridional anisotropy. In general, it seems difficult to significantly improve upon the assumed correlation function without introducing a highly complex non-separable correlation function, while simultaneously guaranteeing both its well-posed form (positive definite on the sphere) and estimating its structure from limited (< 500) data points.

The spatial error magnitudes are assumed to differ over land and ocean, σ_L and σ_O. Together with the correlation function they give a block spatial covariance matrix (*51*),

$$\Sigma_{spatial} = \begin{bmatrix} \sigma_L^2 c_{LL} & \sigma_L \sigma_O c_{LO} \\ \sigma_L \sigma_O c_{LO}^T & \sigma_O^2 c_{OO} \end{bmatrix}, \quad \text{(S6)}$$

where c_{LL}, c_{OO}, c_{LO} matrix blocks give the exponential correlations between land points and other land points, ocean points and ocean points, and land and ocean points, respectively.

The third error term, the nugget, is intended to account for spatially independent errors that are not explicitly accounted for in the reconstruction error Σ_{obs}. These could represent either additional reconstruction error in case the calculated errors are overconfident, or sub-grid scale variability in model error, or some combination of both. The nugget covariance matrix is diagonal since it is spatially independent, but different nugget variances η_L^2 and η_O^2 over land and ocean. It is given by $\Sigma_{nugget} = \mathrm{diag}([\eta_L^2\ \eta_O^2])$, i.e. with two diagonal blocks that are multiples (η_L^2 and η_O^2) of the identity matrix.

6.4 Bayesian Inference

The Bayesian procedure for inferring the joint probability distribution of a vector of unknown parameters θ is to construct the posterior probability distribution

$$p(\theta \mid T_{obs}) \propto L(T_{obs} \mid \theta) p(\theta) \ , \qquad \text{(S7)}$$

where $L(T_{obs}|\theta)$ is the likelihood function giving the probability of observing the data assuming known values of the parameters, and $p(\theta)$ is the prior probability of the parameters. In this case the unknown parameters are taken to be the climate sensitivity as well as the land and ocean spatial errors, $\theta = (ECS_{2xC}, \sigma_L, \sigma_O)$. The correlation length λ, nugget errors η_L and η_O, and biases b_I and b_O are also unknown, but we choose to fix them at assumed values rather than infer them.

The biases are assumed to be zero for reasons discussed above (confounding with ECS_{2xC}). The correlation length and nuggets are fixed to constant values to avoid confounding with σ_L and σ_O. In general, it is difficult to simultaneously estimate the spatial variance, nugget variance, and correlation length of a Gaussian process from limited data. The assumed values are λ = 2000 km, η_L = 2.5 K, and η_O = 0.5 K, chosen from a combination of comparative residual analysis over land and ocean, exploratory variogram analysis, inspection of the likelihood surface at different fixed values, and prior expectations about the range of correlation and the relative amounts of temperature variability between land and ocean. We consider later the effects of varying these assumptions.

The normal likelihood function is given by a multivariate normal distribution,

$$L(T_{obs} \mid ECS, \sigma_L, \sigma_O) = \frac{1}{\sqrt{(2\pi)^n \det \Sigma}} \exp\left[-\frac{1}{2} r^T \Sigma^{-1} r \right], \qquad \text{(S8)}$$

$$r = T_{obs} - [T_{mod}(ECS_{2xC}) + b] \ ,$$

where r is the bias-corrected data-model residual vector.

The prior probabilities of the uncertain parameters are assumed independent of each other. The prior probabilities on the land and ocean spatial errors are assumed to be Lognormal(log(2.5), log(2)/2), i.e., their logarithm is normal with mean log(2.5) and standard deviation log(2)/2, intended to reflect a prior error estimate of 2.5 K uncertain

by a factor of 2 (from 1.25 to 5 K). For climate sensitivity, a bounded uniform prior over the range of modeled ECS_{2xC} values (0.26 to 8.37 K) is assumed for simplicity. While this prior has proven controversial for estimating climate sensitivity from limited instrumental data (e.g. *52, 53*), the inference is presumably less sensitive to the prior in a paleo context with data collected over longer time scales. Furthermore, we consider an alternate prior that is bounded uniform on the climate feedback ($\propto 1/ECS_{2xC}$). The resulting inference for ECS_{2xC} (see Sensitivity Analysis) does not strongly differ between the two priors, and other statistical assumptions have more influence on the inference. Presumably a prior that uses other constraints (such as modern instrumental data) would give an inference for ECS_{2xC} which lies somewhere between the inferences from the uniform ECS_{2xC} and uniform feedback priors, which have prior means — 4.3 and 1.6 K over these bounds, respectively, assuming a 3.7 W m^{-2} forcing for a CO_2 doubling — that are on the upper and lower ends of the ECS_{2xC} ranges found in other studies (*1*).

6.5 Monte Carlo Sampling

Given the posterior probability distribution for the uncertain parameters given by the above likelihood function and priors, the Bayesian inference proceeds by Markov chain Monte Carlo (MCMC) sampling using the Metropolis algorithm. The Metropolis algorithm generates a correlated random walk through parameter space designed so that points in parameter space are visited (sampled) in direct proportion to their calculated posterior probability.

The resulting set of samples from the posterior distribution, the Markov chain, can be used to approximate any quantity of interest (means, quantiles, distributions) by sample statistics (sample means or quantiles, histograms or kernel density estimates). A particular advantage of MCMC method is the ease with which they can compute the marginal distributions of individual parameters from the joint posterior of all uncertain parameters. Theoretically, the marginal distribution of a parameter is obtained by averaging over the uncertainty in all other ('nuisance') parameters, e.g., for climate sensitivity,

$$p(ECS \mid T_{obs}) = \iint p(ECS, \sigma_L, \sigma_O \mid T_{obs}) d\sigma_L \, d\sigma_O \, . \qquad \text{(S9)}$$

With MCMC sampling the desired marginal distribution can be obtained by simply constructing a histogram or density estimate of only the ECS_{2xC} samples in the chain, 'forgetting' about the samples of the other parameters.

A two-stage adaptive Metropolis algorithm is employed in all analyses. First a preliminary chain of 20,000 samples is constructed using informed guesses for the starting point in the chain and for the step sizes proposed for the random walk. Then a second chain of 100,000 samples is constructed, starting at the posterior mean of the first chain, and with a multivariate normal proposal distribution approximately proportional to the sample covariance of the first chain (*54*). This allows the Metropolis algorithm to more efficiently propose moves that are adapted in magnitude and direction to the posterior distribution approximated by the first, possibly poorly converged chain. Only the second, adapted chain is used in further analysis.

The resulting chains appear well converged in graphical diagnostics, have reasonable acceptance rates for proposed moves in the random walk (41% for the default

analysis), and have reasonable effective sample sizes (between 6000 and 7000 for the three parameters estimated in the default analysis).

6.6 Joint Posterior

The posterior inferred from the proxy data is given in Figure S13. The marginal distribution for ECS_{2xC} is peaked near the posterior mean of 2.2 K, and is multimodal. This multimodality could be partly due to the non-smooth linear interpolation of the model emulator, but also may reflect real physical behavior of the model (for example, the collapse of the AMOC near ECS_{2xC} = 2.7 K). The estimated spatial errors are around 3.5 K over land and 1.5 K over ocean. The joint posterior shows little correlation (confounding) between ECS_{2xC} and the two spatial error parameters.

7. Sensitivity Tests

A number of experiments are performed to examine the sensitivity of the inference to statistical and physical assumptions. These tests, which are summarized graphically in Figures S14 and S14, are described below. In addition to the tension between land and ocean based estimates of ECS_{2xC}, the inferred ECS_{2xC} distribution has some sensitivity to assumptions about bias, nugget variance, and correlation length, as well as dust forcing and sea level SST corrections. Wind stress forcing narrows the uncertainty range but does not significantly change the mean estimate.

7.1 Land/Ocean

The analysis is applied to only the land or only the ocean data. The ocean-only inference for ECS_{2xC} is similar to the combined inference, with a range of about 1.5 to 3 K, indicating that the ocean data dominate the land data in the inference. The land-only inference supports significantly higher climate sensitivities, roughly similar to the 2 to 4.5 K IPCC range.

7.2 Dust Forcing

In order to account for the uncertainty in dust forcing we have estimated the surface temperature response to dust forcing using a subset of 11 models with different ECS_{2xC} and performed an additional LGM experiment for each of those models without dust radiative forcing. Assuming a linear response to dust forcing, we interpolated between these simulations to fill in the additional ECS_{2xC} values for which no experiments had been performed (0×Dust). Then we extrapolated (doubled) the surface temperature response to estimate two times larger dust forcing (2×Dust). The results from shown that increasing the dust forcing implies a lower ECS_{2xC} (below 2 K) while eliminating the dust forcing implies a higher ECS_{2xC} (near 3 K).

7.3 Wind Stress Forcing

The UVic model uses prescribed wind stress at the sea surface in order to force the ocean and sea ice model components. In the standard model we use present day wind stress. In order to account for changes in winds at the LGM we applied an anomaly (LGM minus LH) calculated from the coupled ocean-atmosphere general circulation model GENMOM (*49*). Monthly mean anomalies were added to the seasonal climatology of the wind stress fields.

In both cases the inference with wind stress corrections favors ECS_{2xC} near 2 K, as

in the default analysis, but with reduced uncertainty. The AMOC is significantly stronger in models with GENMOM wind stress forcing (Figure S6) in the LGM run than in the LH run, a result that may be inconsistent with deep ocean carbon isotope paleo-data (*48*), indicating possible structural model uncertainty.

7.4 Sea Level SST Correction

The correction of $\Delta SST_{SL} = 0.32$ K added to the simulated SST in order to account for the lower sea level during the LGM was estimated by one additional model simulation as described in section 6. The value of 0.32 K is only half of what one would expect from a simple application of a constant lapse rate of 6 K/km. Uncertain model parameters, such as the application of a reduction of the lapse rate in the calculation of outgoing longwave radiation over topography (this parameter is called *rfactor* in the UVic model version 2.8 source code) may be the reason for this deviation and suggest that the model derived value may be uncertain. We address this uncertainty by varying ΔSST_{SL} from 0 to 0.64.

Lower ECS_{2xC} (below 1.5 K) is favored in the absence of the sea level correction, whereas higher ECS_{2xC} (2 to 3 K) is favored by a larger SST correction.

We have performed additional model experiments with the fully coupled ocean-atmosphere general circulation model OSUVic at T42 resolution as described in (*55*). For these experiments we used PMIP3 boundary conditions for ice sheets and atmospheric CO_2 and use present day sea level in one experiment and 120 m lower sea level in the other. The differences between these two models therefore quantify the effect of the sea level lowering on SSTs. Because the model is computationally expensive it was integrated only for 240 years. Global mean sea surface temperature difference between the two simulations is 0.3 K between model years 200 and 240. Global marine surface air temperatures are $\Delta SAT_{SL} = 0.46$ K warmer.

Inspection of the spatial distribution shows that over 72% of the surface ocean SSTs are between 0.22 and 0.42 K warmer in the simulation with lower sea level, mainly between 40°S and 40°N. At higher latitudes in the North Atlantic and North Pacific the differences are larger and over the Southern Ocean high latitudes and the Arctic they are smaller. These independent results confirm our best estimate of 0.32 K for the global SST sea level correction.

7.5 North Atlantic Data

The North Atlantic region where the effects of an AMOC collapse in the model (Fig. S6) are strongest is excluded from the analysis, as described in the Data-Model Comparison section 5. This favors lower ECS_{2xC} between 1 and 2 K. Inspection of frequency distributions of temperature anomalies, analogous to Fig. S9 but excluding the North Atlantic region, shows that the main peaks increase for the observations and all models, while cold temperature anomalies (below 3 K for the observations and below −2 K, −3.5 K, and −4.5 K for models with ECS_{2xC} equal to 2 K, 3 K, and 4 K, respectively) become less abundant, and the secondary maximum around −3.5 K for model ECS_{2xC}=2 disappears. This way the temperature distributions at low low ECS_{2xC} change from bimodal to unimodal and become more similar to the observed distribution when the North Atlantic region is excluded from the comparison, whereas at high ECS_{2xC} the temperature distributions, without this bimodality, are relatively unchanged in shape. We

speculate that this causes lower ECS_{2xC} values to receive higher probability weights in the Bayesian analysis. This sensitivity test indicates that North Atlantic cooling is an influential constraint, favoring higher ECS_{2xC} values. It demonstrates that excluding regions can lead to a biased ECS_{2xC} estimate, a result that emphasizes the importance of good spatial data coverage.

7.6 Statistical Assumptions

Bias: Four experiments assume nonzero bias over land or ocean of ±0.5 K. The ocean bias has a particularly strong influence, altering the ECS_{2xC} estimate by about 1 K. The influence of ocean bias is larger than the influence of land bias, due to the ocean data's overall influence on the inference.

Nugget Variance: The assumed nugget error of 2.5 K over land and 0.5 K over ocean is changed to zero over land and ocean (no nugget), or to 3.5 K over land or 1.5 K over ocean (large nugget). Eliminating the nugget implies a larger ECS_{2xC} but produces an extremely narrow uncertainty range, suggesting a mis-specified statistical model. Increasing the nugget eliminates ECS_{2xC} below 2 K but otherwise leaves the posterior unchanged.

Spatial correlation: The assumed correlation length scale of 2000 km is changed to 1000 km or 5000 km. The long correlation length eliminates ECS_{2xC} below 2 K; the short correlation length favors low ECS_{2xC} near 1 K.

Observation error: This sensitivity test explores the role of error specification, in particular the influence of model error and spatial auto-correlation. Here the analysis is repeated neglecting spatial correlation and model error and assuming only spatially independent observation errors. This gives a very narrow ECS_{2xC} distribution peaked near 3.4 K. The extreme sharpness of the distribution indicates a mis-specification of the statistical model (i.e., it is overconfident due to neglecting model error and spatial dependence).

Spatial error: The analysis is performed assuming only spatially correlated errors (land and ocean variances are estimated from the residuals as in the default analysis), neglecting observation error and the nugget error. This gives a sharp ECS_{2xC} mode near 3 K, although with some probability down to 1 K. The sharp peak also suggests mis-specification (i.e., observation and nugget errors are important).

Heavy tailed likelihood: To explore the possibility of non-normally distributed errors, a multivariate Student-t likelihood is used in place of the multivariate normal likelihood. This distribution has 3 degrees of freedom and has a covariance equal to the covariance assumed in the multivariate normal analysis. This slightly favors lower ECS_{2xC} values but otherwise leaves the ECS distribution unchanged.

Climate sensitivity prior: A prior that is uniform on the climate feedback factor F_{2x}/ECS_{2xC} is used instead of the uniform prior on climate sensitivity. This prior favors slightly lower ECS_{2xC} values but leaves the ECS_{2xC} posterior distribution essentially unchanged.

Outliers excluded: Some grid cells have reconstructed temperature anomalies that are as many as 6 standard deviations away from the (posterior mean) modeled anomalies. To test the sensitivity of the inference to the presence of outliers, grid cells with

reconstructed anomalies more than 3 standard deviations away from the ECS_{2xC} = 2.51 K model run are excluded. This criterion excludes 8 grid cells, all land cells in North America. The exclusion of outliers has negligible effect on the inference.

7.7 Other Uncertainties

Our study does not provide a complete uncertainty assessment. We have taken into account a number of known important uncertainties such as dust forcing. Others, however, are not included, for example uncertainties in the reconstruction of the ice sheets and vegetation cover. Also our model ensemble does not scan the full parameter space. For example, changes in shortwave radiation due to clouds are not taken into account. Our statistical method does not explicitly consider bias due to limited data coverage.

8. Vegetation Simulation

Our simulations include the influence of climate and atmospheric CO_2 concentrations on the vegetation distribution. Figure S10 shows that the largest changes in simulated vegetation occur at northern hemisphere high latitudes. The simulated dramatic reduction of the boreal/temperate forest in the northern hemisphere extra-tropics from 1.8×10^{-7} km^2 to 0.4×10^{-7} km^2 is consistent with pollen reconstructions and previous offline vegetation modeling (*56*). The extent of tropical forest decreases in the model from 2.7×10^{-7} km^2 to 2.4×10^{-7} km^2 is qualitatively consistent with, but quantitatively much less, than simulated by (*56*) who find reductions of $(1.1\pm0.3)\times10^{-7}$ km^2. Globally the area covered by C_3 grass decreases by 10% (from 4.0×10^{-7} km^2 to 3.6×10^{-7} km^2) whereas C_4 grass coverage increases by 20% (from 1.1×10^{-7} km^2 to 1.3×10^{-7} km^2) consistent with the competitive advantage of C_4 photosynthesis under low CO_2.

Tables

Table S1 Shakun et al. (*44*) compilation of reconstructed LGM surface temperature anomalies. This dataset is available for download at http://mgg.coas.oregonstate.edu/~andreas/data/schmittner11sci

Location	Core	Proxy	Ref.	Lat (°)	Lon (°)	Elev./ Depth (m)	19-23 ka T	0-2 ka T	WOA 98 T	LGM ΔT	Error	MARGO			
												Lat	Lon	LGM anom	total error
GISP2, Greenl.	-	ice core $\delta^{18}O$ and boreh. temp	(*57*)	72.6	-38.5	3207	-47.1	-31.6		-15.5	2.3				
NE Atlantic	NA 87-22	foram assembl	(*58*)	55.5	-14.7	-2161	6.4	13.5	11.4	-7.0	5.1	57.5	347.5	-5.9	5.1
NE Atlantic	MD01-2461	Mg/Ca	(*59*)	51.8	-12.9	-1153	8.7		12.5	-3.8	1.9				
central N Atlantic	CH 69-09	foram assembl	(*58*)	41.8	-47.4	-4100	16.3	16.4	15.4	-0.2	2.5				
Japan margin	PC-6	UK'37	(*60*)	40.4	143.5	-2215	12.9	15.7	11.5	-2.9	3.0				
Iberian margin	SU81-18	foram assembl	(*58*)	37.8	-10.2	-3135	17.0		17.6	-0.6	2.2	37.5	347.5	-3.7	2.2
N Pacific	MD01-2421	UK'37	(*61*)	36.0	141.8	-2224	17.4		19.6	-2.3	1.9	37.5	142.5	-3.0	1.9
Chinese loess pl.	Section MS2008E	MBT/ CBT	(*62*)	34.9	113.3	~200	15.6	23.4		-7.8	1.9				
Japan margin	KT92-17 St. 14	UK'37	(*63*)	32.6	138.6	-3252	21.5		22.2	-0.7	3.0				
Blake outer ridge	KNR140-51GGC	Mg/Ca	(*64*)	32.6	-76.3	-1790	25.6		24.6	1.0	2.0				
Nile Delta	GeoB 7702-3	TEX86	(*65*)	31.7	34.1	-562	15.9	26.8	21.9	-10.9	4.3	32.5	32.5	-5.1	4.3
East China S	MD98-2195	UK'37	(*66*)	31.6	129.0	-746	20.6	23.6	22.4	-3.0	2.0				
Gulf of Mexico	MD02-2575	Mg/Ca	(*67*)	29.0	-87.1	-847	22.6	25.4	24.3	-2.8	1.9				
Red Sea	GeoB 5844-2	UK'37	(*68*)	27.7	34.7	-963	23.1	26.7	25.3	-3.7	2.0				
Gulf of Mexico	EN32-PC6	Mg/Ca	(*69*)	27.0	-91.3	-2280	23.6		25.1	-1.5	3.8	27.5	267.5	-4.0	3.8
NWAfrican margin	ODP 658C	foram assembl	(*70*)	20.8	-18.6	-2263	15.2	20.8	20.3	-5.5	1.9	22.5	342.5	-2.3	1.9
S. China Sea	ODP 1144	Mg/Ca	(*71*)	20.1	117.6	-2037	23.6	27.2	26.4	-3.6	1.6	22.5	117.5	-3.2	1.6
Arabian Sea	74KL	UK'37	(*72*)	14.3	57.3	-3212	25.0	27.2	26.6	-2.1	1.1	12.5	57.5	-1.5	1.1
Arabian S	74KL	TEX86	(*72*)	14.3	57.3	-3212	24.4	27.4	26.6	-3.0	1.1	12.5	57.5	-1.8	1.1
Western Caribbean Sea	VM28-122	Mg/Ca	(*73*)	11.6	-78.4	-3623	24.1		27.7	-3.6	1.7	12.5	282.5	-4.0	1.7
Arabian Sea	NIOP-905	UK'37	(*72*)	10.8	51.9	-1567	25.4	26.3	26.0	-0.9	1.2	12.5	52.5	-1.2	1.2

Arabian Sea	NIOP-905	TEX86	(*72*)	10.8	51.9	-1567	22.7	26.2	26.0	-3.5	1.4	12.5	52.5	-1.5	1.4
E eq. Pacific	MD02-2529	UK'37	(*74*)	8.2	-84.1	-1619	26.0	29.1	28.2	-3.1	2.5				
E eq. Pacific	ME0005A-43JC	Mg/Ca	(*75*)	7.9	-83.6	-1368	24.0		28.2	-4.3	1.5				
S China Sea	MD01-2390	UK'37	(*76*)	6.6	113.4	-1545	26.7		28.4	-1.8	1.4	7.5	112.5	-2.9	1.4
S China Sea	MD01-2390	Mg/Ca	(*76*)	6.6	113.4	-1545	24.6	27.6	28.4	-3.0	1.2	7.5	112.5	-2.9	1.2
Gulf of Guinea	MD03-2707	Mg/Ca	(*77*)	2.5	9.4	-1295	23.1	25.8	27.6	-2.7	1.5				
E eq. Atlantic	GeoB 4905	Mg/Ca	(*78*)	2.5	9.4	-1328	24.2	26.1	27.6	-1.9	1.5				
E eq. Pacific	ME0005A-24JC	UK'37	(*79*)	0.0	-86.5	-2941	23.3		24.3	-1.0	1.3	2.5	272.5	-1.7	1.3
E eq. Pacific	V21-30	UK'37	(*80*)	-1.2	-89.7	-617	24.1		22.8	1.3	6.4	-2.5	272.5	-2.7	6.4
E eq. Pacific	V19-28	UK'37	(*81*)	-2.4	-84.7	-2720	21.9	24.0	22.7	-2.1	3.5	-2.5	277.5	-2.6	3.5
Brazilian margin	GeoB 3910	UK'37	(*81*)	-4.2	-36.3	-2362	25.9	27.1	27.3	-1.2	0.9	-2.5	322.5	-1.4	0.9
Western tropical Atlantic	GeoB 3129	Mg/Ca	(*82*)	-4.6	-36.6	-830	24.6	27.3	27.3	-2.7	0.9	-2.5	322.5	-1.6	0.9
West Pacific	MD98-2176	Mg/Ca	(*83*)	-5.0	133.4	-2382	26.2	28.8	28.2	-2.6	2.5				
Congo Basin	GeoB 6518-1	MBT/CBT	(*84*)	-2.0	22.0	999999	20.9	24.9		-4.0	1.9				
Gulf of Guinea	GeoB 6518-1	UK'37	(*85*)	-5.6	11.2	-962	22.5	24.6	24.4	-2.1	2.3	-7.5	12.5	-3.2	2.3
Lake Tanganyika	NP04-KH3, NP04-KH4	TEX86	(*86*)	-6.7	29.6	773	24.0	27.5		-3.5	1.5				
West Pacific	MD98-2165	Mg/Ca	(*87*)	-9.7	118.4	-2100	24.6	27.1	27.8	-2.5	2.5				
West Pacific	MD98-2170	Mg/Ca	(*83*)	-10.6	125.4	-832	26.6		28.4	-1.8	1.9				
Timor Sea, Indian Ocean	MD01-2378	Mg/Ca	(*88*)	-13.1	121.8	-1783	25.2	28.0	28.3	-2.8	1.0	-12.5	122.5	-1.4	1.0
Subtropical SE Atlantic	ODP 1084B	Mg/Ca	(*89*)	-25.5	13.0	-1992	11.4	13.5	16.2	-2.1	1.5	-27.5	12.5	-0.7	1.5
Brazilian margin	KNR159-5-36GGC	Mg/Ca	(*64*)	-27.5	-46.5	-1268	23.8		23.2	0.6	1.8	-27.5	312.5	-1.2	1.8
Chilean margin	GeoB 7139-2	UK'37	(*90*)	-30.2	-72.0	-3270	14.9		15.5	-0.5	3.0				
South Australia	MD03-2611	UK'37	(*91*)	-36.7	136.7	-2420	11.0	18.2	16.2	-7.2	3.0				
New Zealand	MD97-2121	UK'37	(*92*)	-40.4	178.0	-3014	13.2		16.6	-3.4	1.3	-42.5	177.5	-3.2	1.3
Chilean margin	ODP 1233	UK'37	(*93*)	-41.0	-74.5	-838	9.4		13.3	-3.9	2.0				
SE Atlantic	TN057-21-	UK'37	(*94*)	-41.1	7.8	-4981	14.5		11.2	3.3	2.6				

	PC2														
SE Atlantic	TN057-21	Mg/Ca	(*95*)	-41.1	7.8	-4981	10.3		11.2	-0.9	2.0				
New Zealand	SO136-GC11	UK'37	(*96*)	-43.5	167.9	-1556	9.6		14.5	-4.9	1.0	-42.5	167.5	-4.6	1.0
New Zealand	MD97-2120	UK'37	(*92*)	-45.5	174.9	-1210	6.6		11.0	-4.4	3.4	-47.5	172.5	-6.7	3.4
EDML, Antarct.	-	ice core δ18O	(*97, 98*)	-75.0	0	2892	-7.4	0.0		-7.4	1.1				
Dome C, Antarct.	-	ice core δ18O	(*97, 98*)	-75.1	123.4	3240	-9.3	0.0		-9.3	1.4				
Dome Fuji, Antarct.	-	ice core δ18O, δD	(*99*)	-77.3	39.7	3810	-8.2	0.0		-8.2	1.2				
Vostok, Antarct.	-	ice core δD	(*100*)	-78.5	108	3500	-8.1	0.0		-8.1	1.2				

Figures

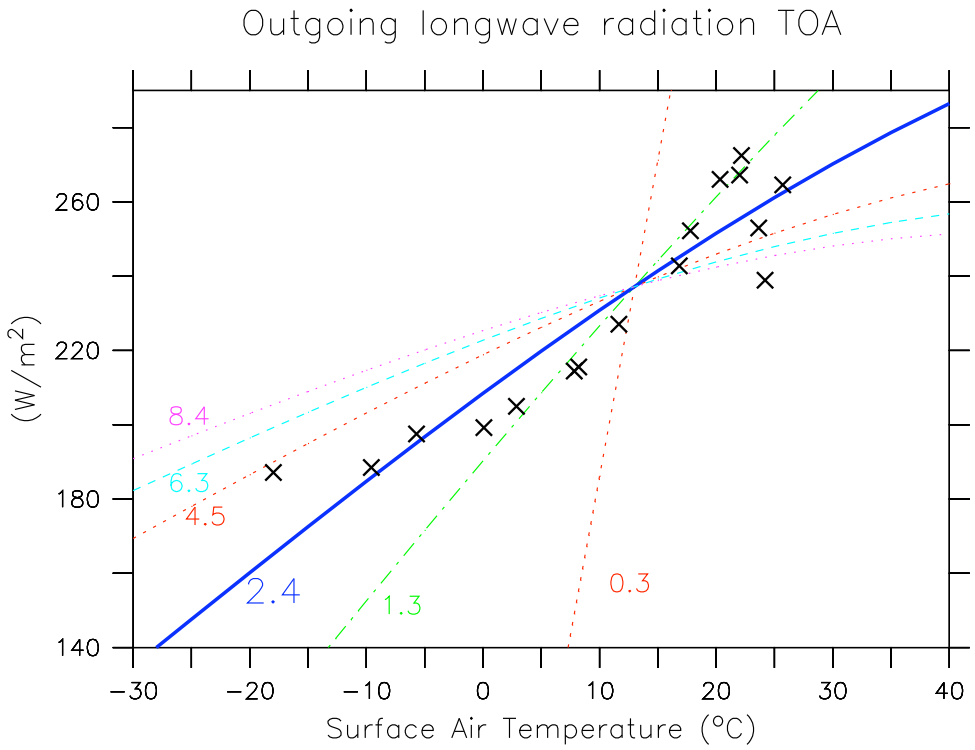

Figure S1: Outgoing longwave radiation Q_{PLW} at the top-of-the-atmosphere as a function of surface air temperature T_a. Colored lines show results of the parameterization by Thompson and Warren (1982) (equation S1) with different slopes and approximately constant T_a at its preindustrial value of 13°C. Colored numbers denote the ECS_{2xC} of the different model versions. Symbols show near-surface (2 m) air temperature data from the NCEP reanalysis (*101*) and longwave radiation from ERBE satellite measurements (*102*) averaged over 10 degree latitudinal bands.

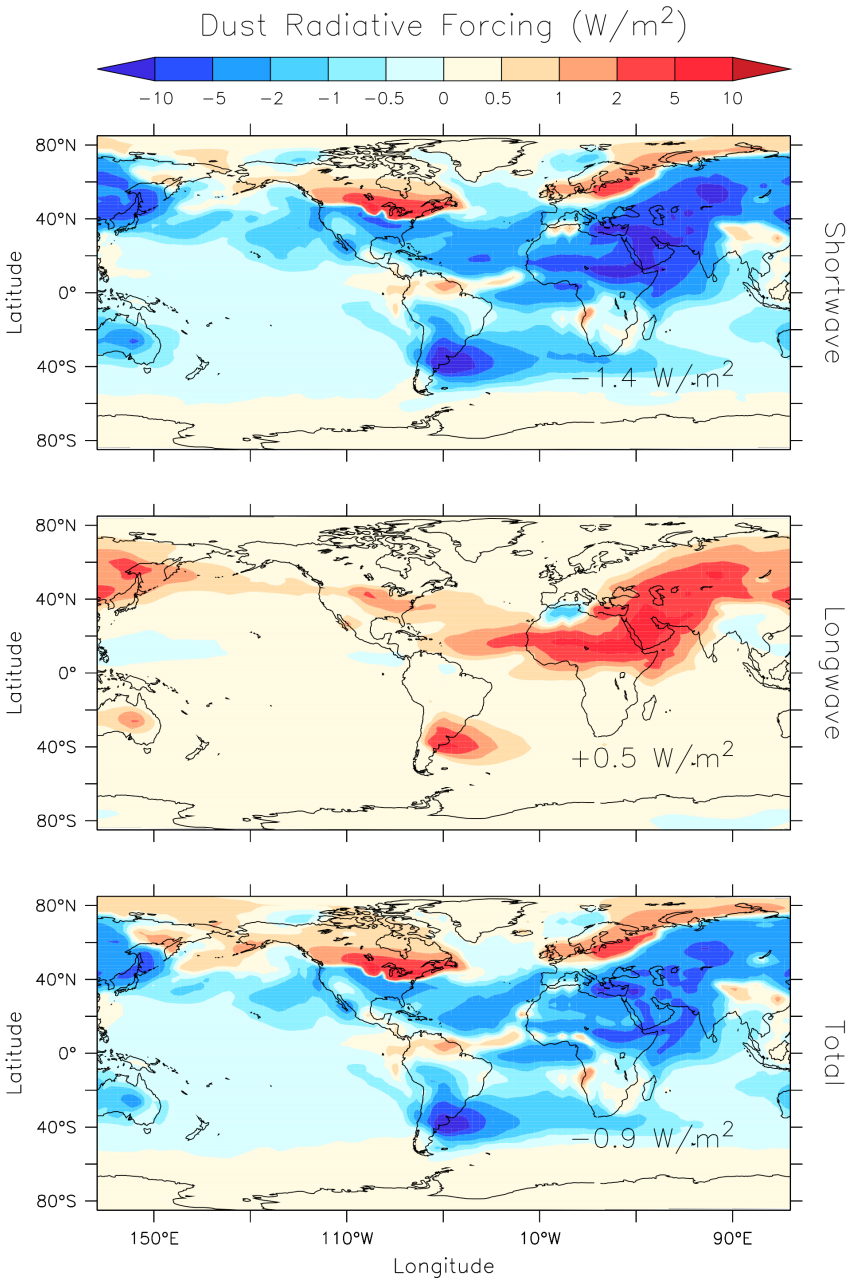

Figure S2: Annual mean dust forcing (LGM minus pre-industrial) as a function of longitude and latitude used as a perturbation to the fluxes at the top-of-the-atmosphere in the UVic model. Top: shortwave forcing, center: longwave forcing, bottom: total (shortwave plus longwave) forcing. Negative (blue) values denote a cooling influence, positive (red) a warming. From (*34*).

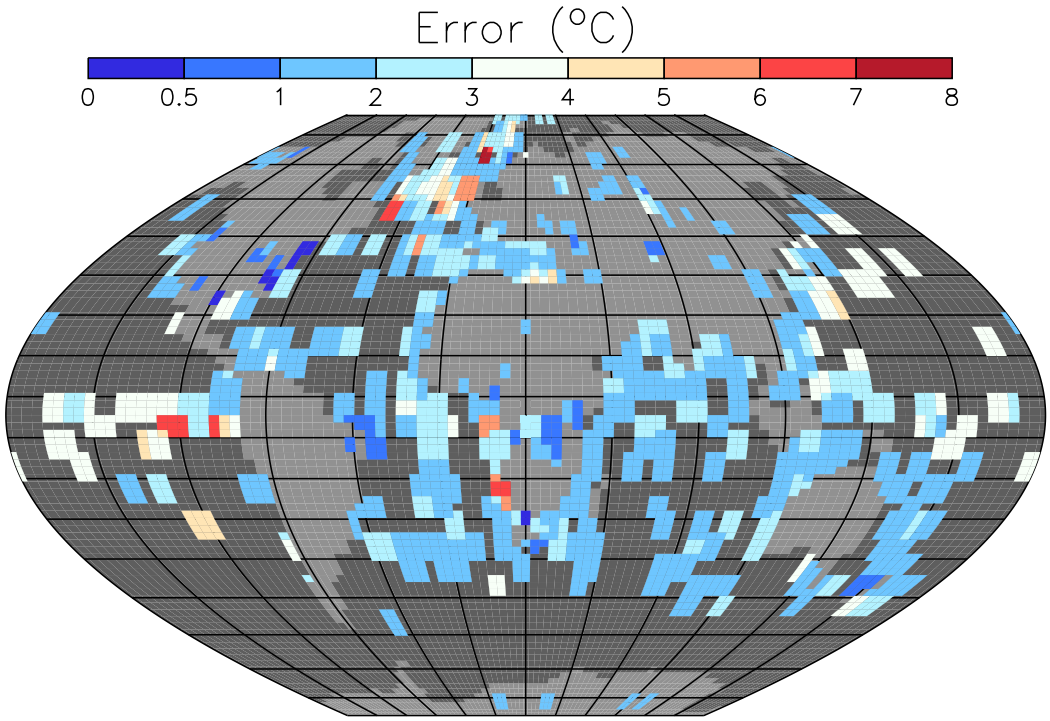

Figure S3: Error in the LGM temperature reconstructions as reported in the original publications (*12, 13, 44*).

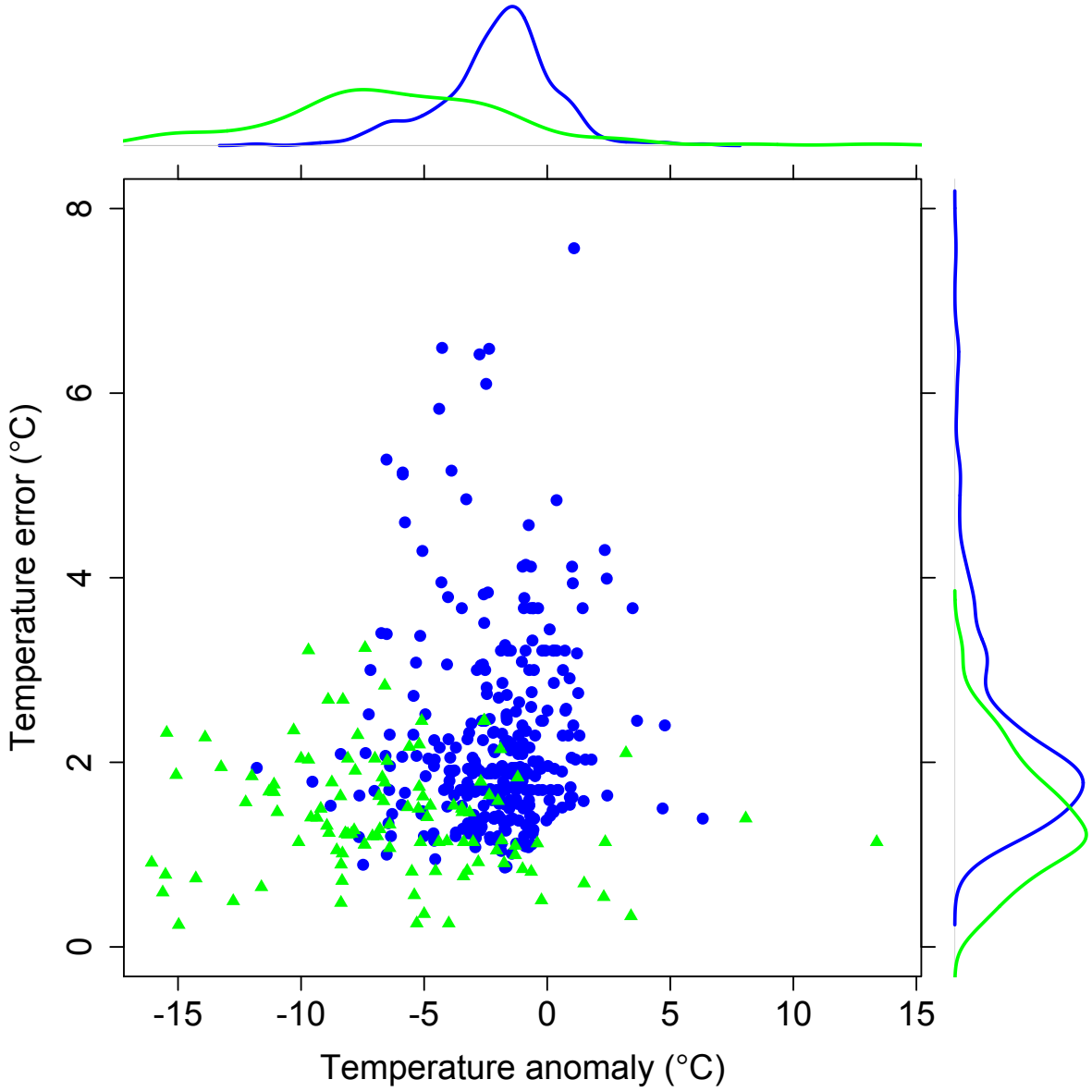

Figure S4: Scatterplot of reconstruction error vs. reconstructed temperature anomaly for land (green) and ocean (blue) data, along with marginal distributions of temperature errors (top) and temperature anomalies (right).

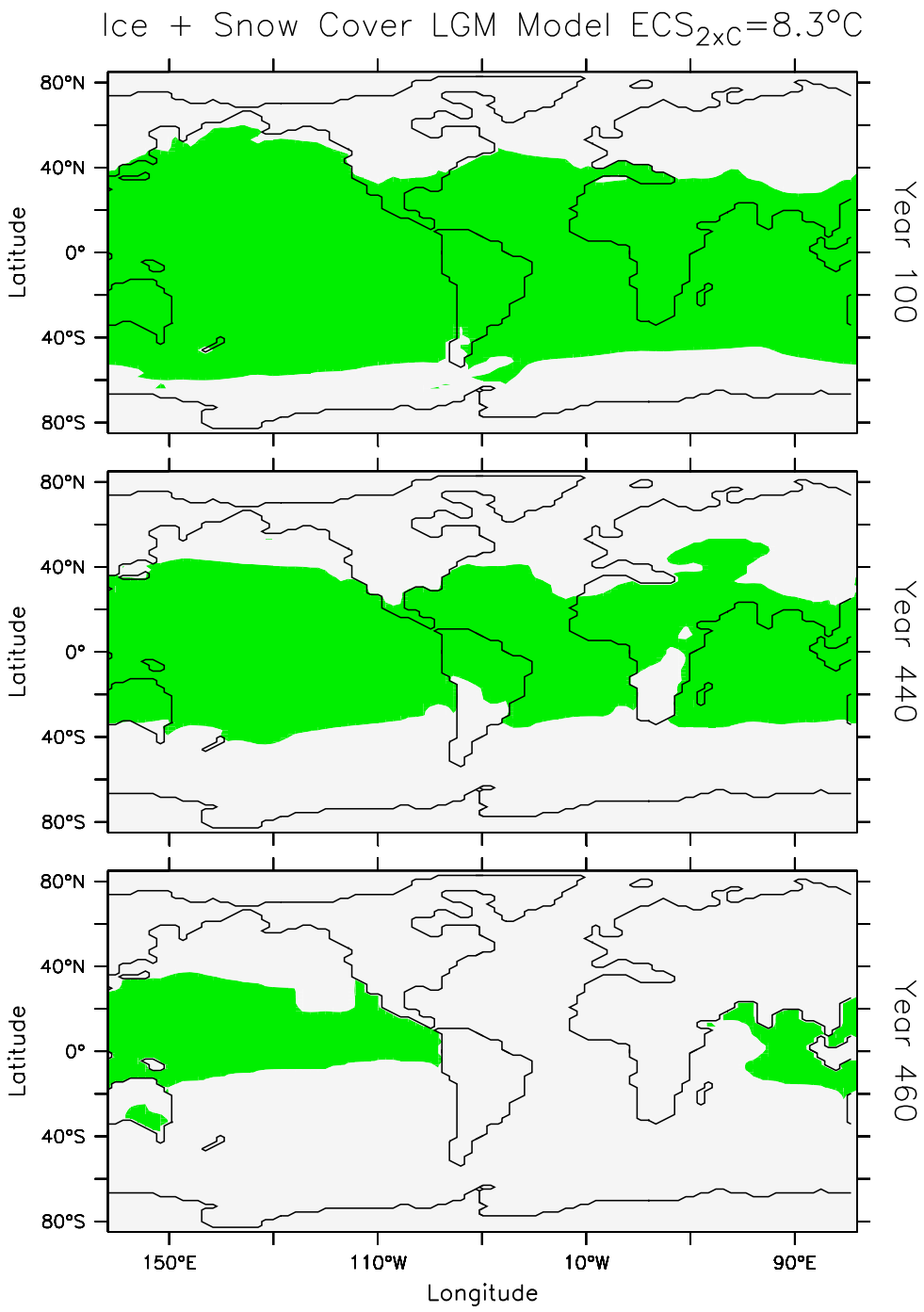

Figure S5. Annual mean snow and ice cover (white) in the LGM experiment with a ECS_{2xC}=8.3 K at different times during the integration. Top: 100 model years after the switch to LGM boundary conditions, center: 440 years, and bottom: 460 years.

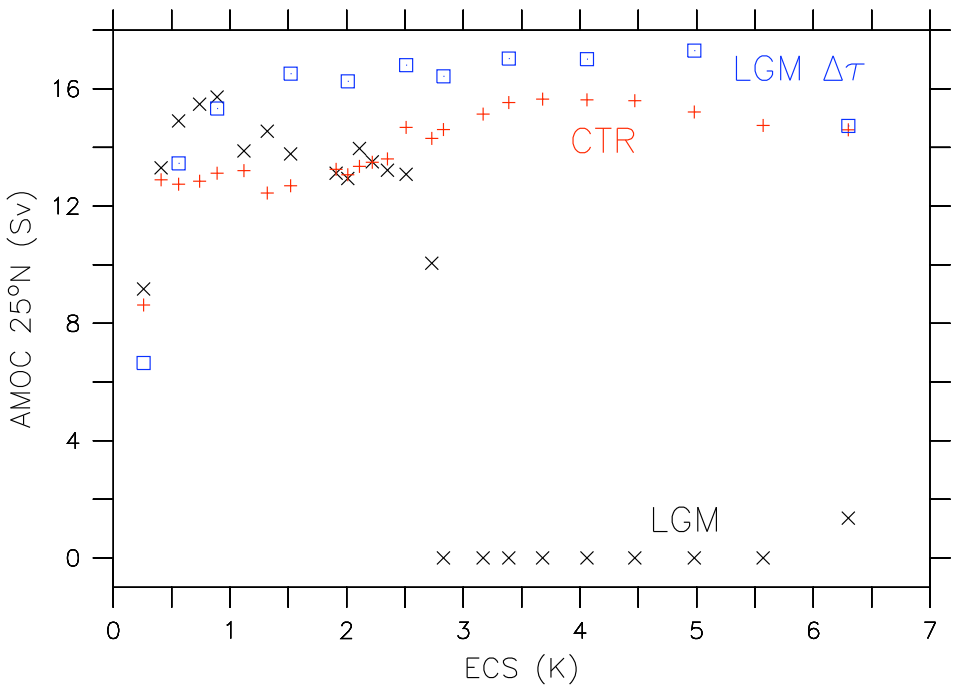

Figure S6. Simulated Atlantic Meridional Overturning Circulation (AMOC) at 25°N as a function of the climate sensitivity. Results from the pre-industrial control simulation are shown as red crosses, LGM results as black xes and results from LGM experiments with wind stress from GENMOM as blue squares.

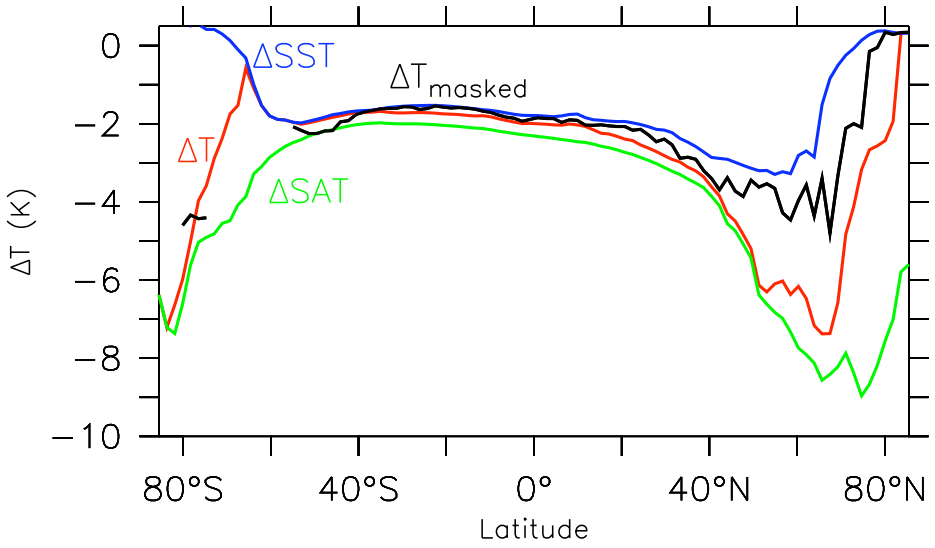

Figure S7: Zonally averaged surface temperature changes (LGM minus LH) from the best-fitting model (ECS_{2xC}=2.4 K). Black: surface temperature (SST over the ocean corrected for sea level lowering by adding 0.3 K, and SAT over land) masked by the grid points that contain reconstructions. Red: unmasked surface temperature (SST over the ocean and SAT over land). Green: unmasked SAT. Blue unmasked SST.

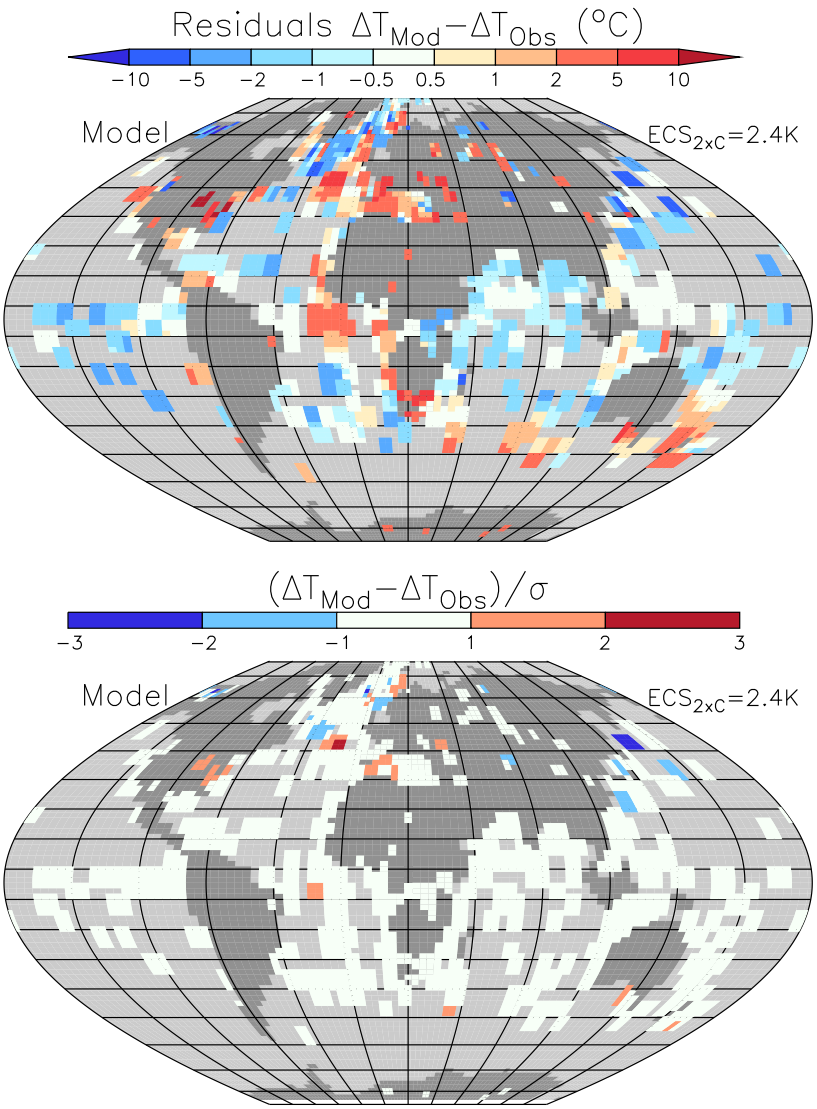

Figure S8: Map of residuals (difference in temperature change between model and reconstructions, top) from the best fitting model (ECS_{2xC} = 2.4 K) and residuals divided by the combined error $\sigma=\sigma_O+\sigma_M$, where σ_O is the published observation error shown in Figure S3 and σ_M is the estimated model error (6 K over land and 2 K over the ocean), which consists of the correlated error (3.5 K over land and 1.5 K over the ocean) and the nugget error (2.5 K over land and 0.5 K over the ocean).

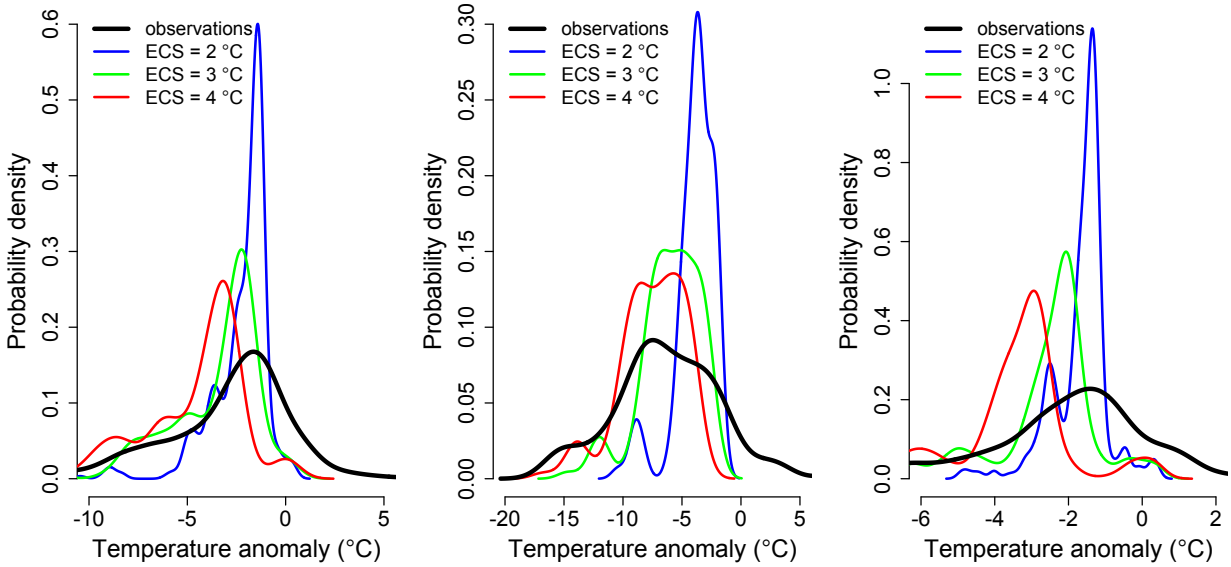

Figure S9: Distributions of reconstructed (observed) and modeled LGM-modern temperature anomalies at selected climate sensitivities, for land and ocean (left), land only (center), and ocean only (right) grid cells.

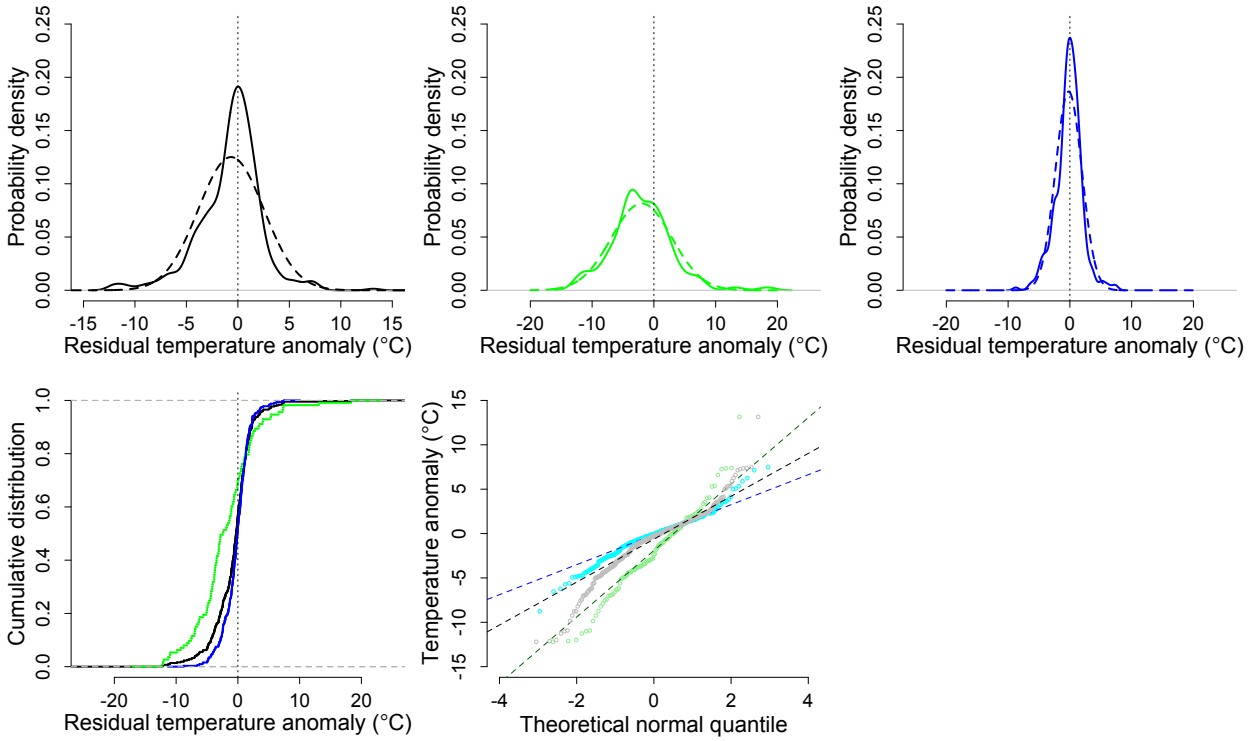

Figure S10: Residuals at the posterior mean climate sensitivity (2.2 K) for land and ocean (upper left), land only (upper center), and ocean only (upper right) grid cells, with normal fits (dashed lines) superimposed. Also shown are cumulative distribution functions of the residuals (lower left) and normal Q-Q plots (lower center) with linear fits between the first and third quartiles (dashed lines).

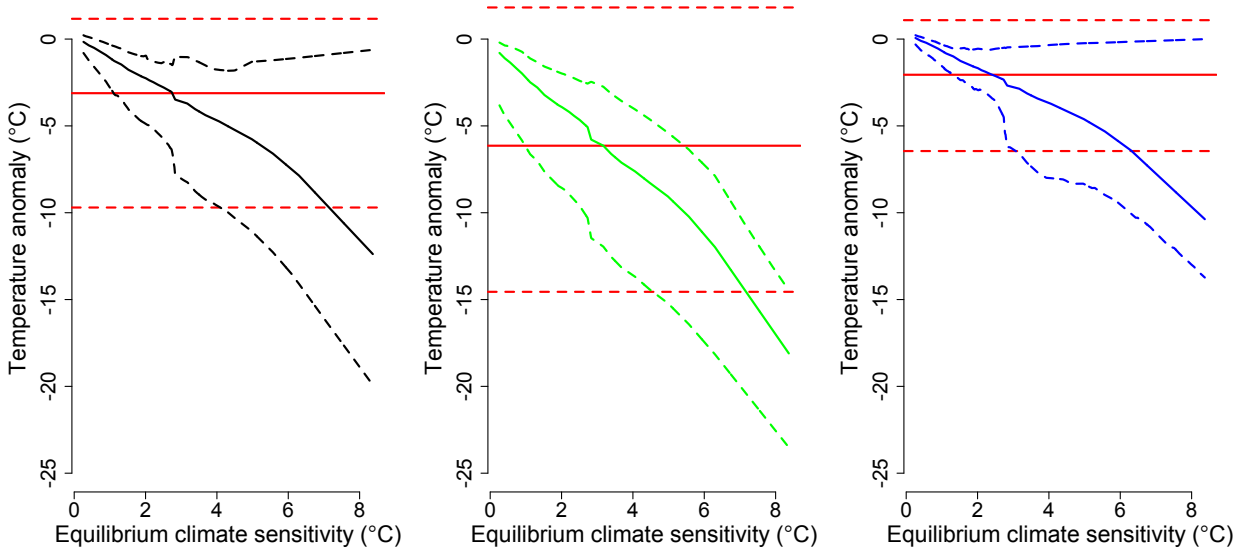

Figure S11: Plot of mean and 90% interval for the reconstructed temperature anomaly (solid and dashed red lines) and mean and 90% intervals for the modeled temperature anomaly as a function of ECS_{2xC} for land and ocean (left, black), land only (center, green), and ocean only (right, blue) grid cells.

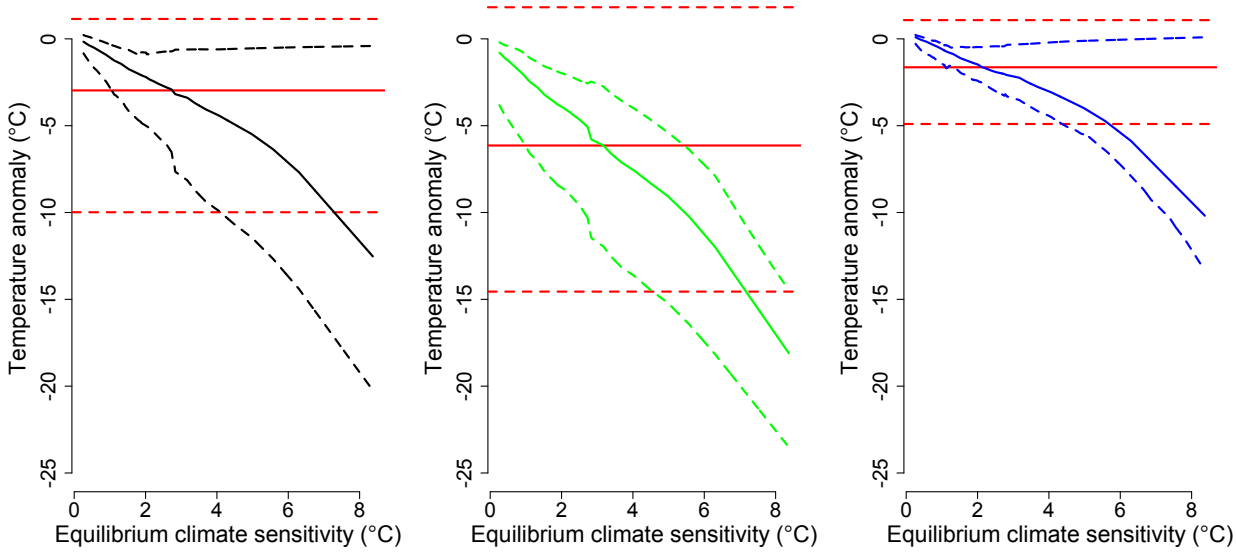

Figure S12: As in Figure S11, but with grid cells in the North Atlantic region omitted.

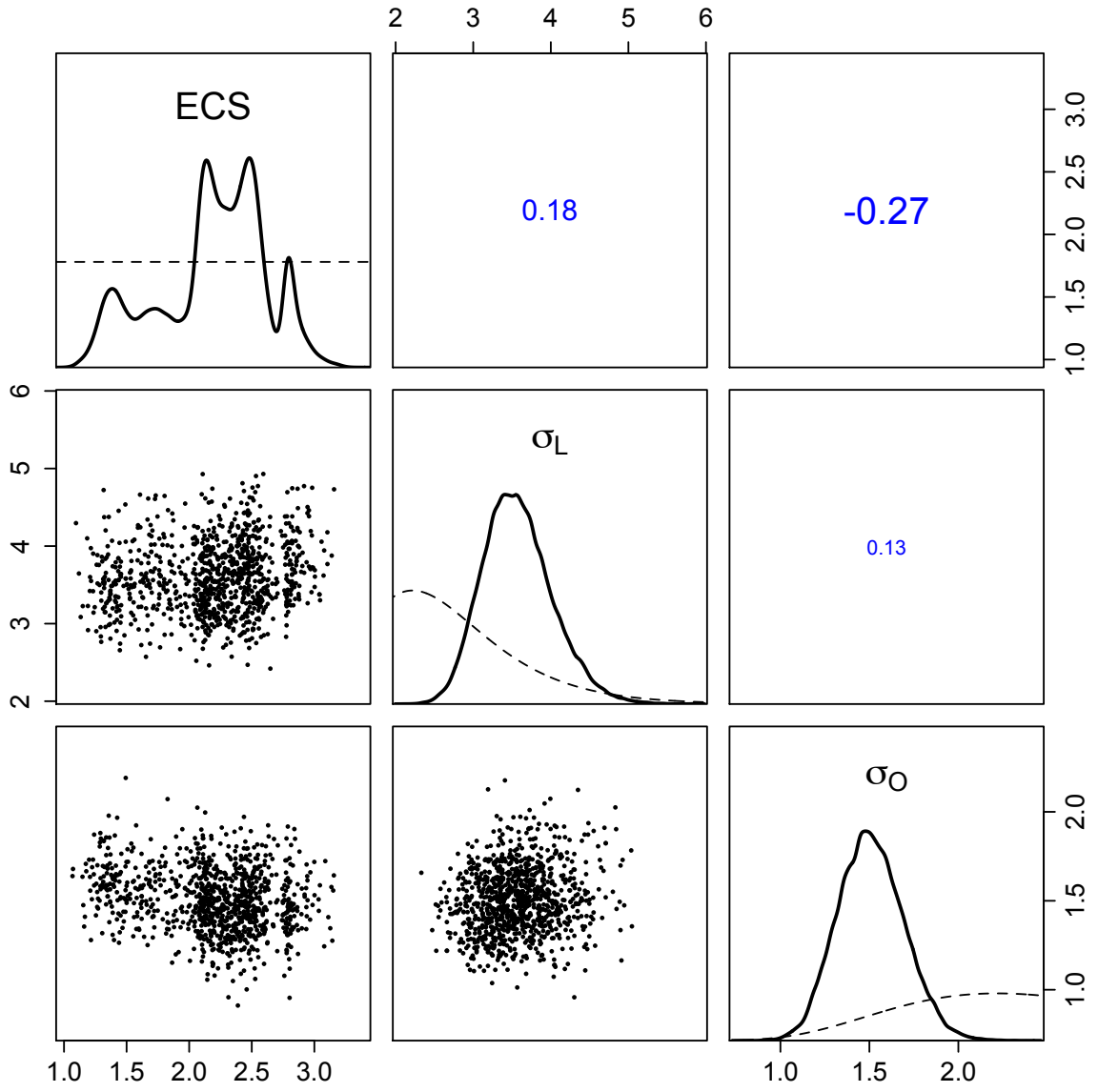

Figure S13: Marginal and pairwise joint posterior distribution of estimated parameters (ECS_{2xC}, land spatial error, and ocean spatial error), for the default analysis. The marginal distributions are given on the diagonal (with priors given by dashed curves), with pairwise scatterplots of posterior samples given below the diagonal, and pairwise correlations above the diagonals. All units are in K.

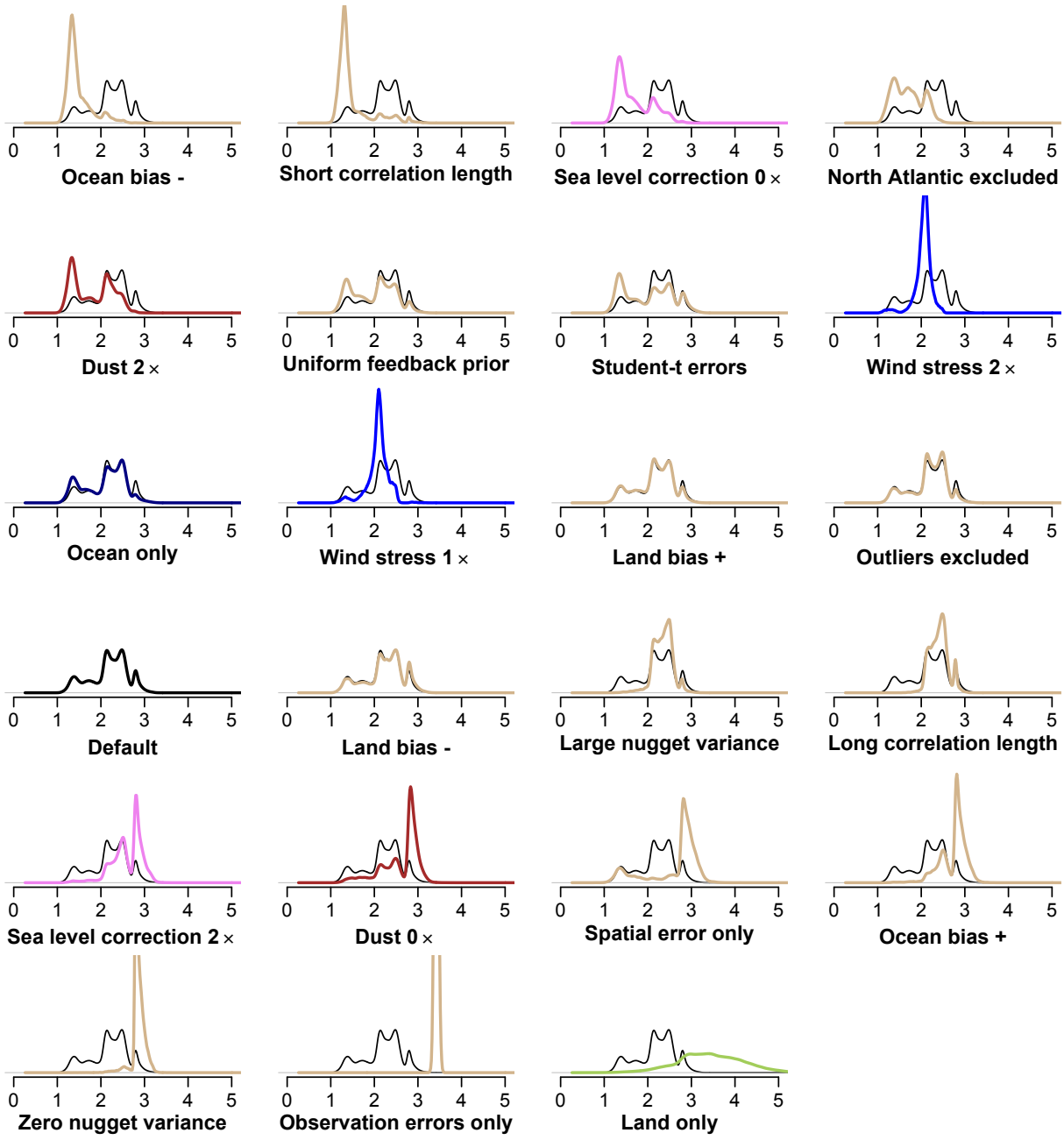

Figure S14: Marginal posterior probability distributions for ECS_{2xC} estimated in each sensitivity experiment (colored curves) compared to the distribution obtained in the default analysis (thin black curve), sorted by increasing mean ECS_{2xC}.

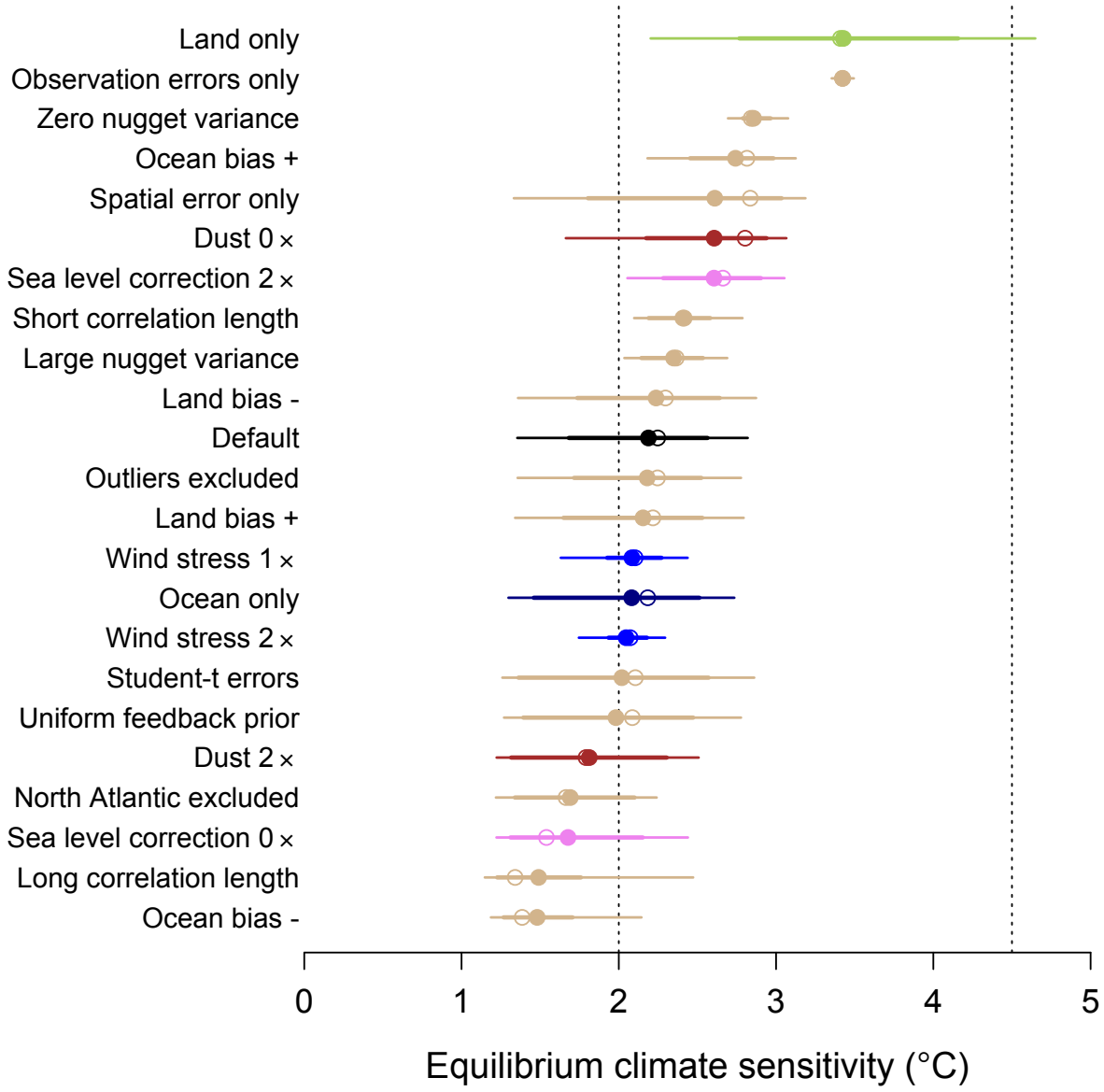

Figure S15: Mean and median (filled and open circles) ECS_{2xC} values, along with 66% and 90% intervals (thick and thin lines) for the various sensitivity experiments (as in Figure S14), sorted by decreasing mean ECS_{2xC}. The vertical dotted lines are the IPCC range of 2–4.5 K.

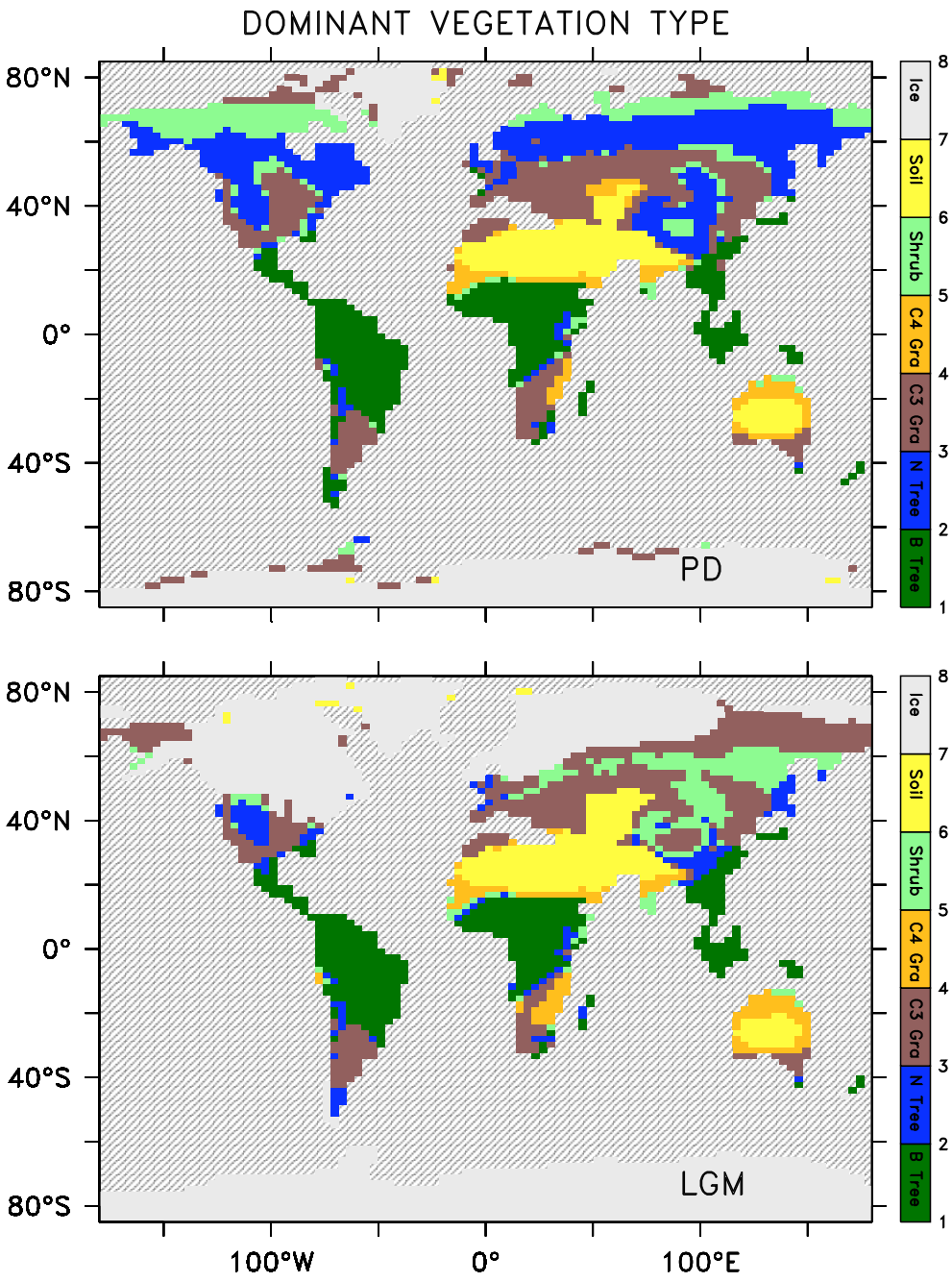

Figure S16: Simulation of dominant vegetation type for the present day (top) and the LGM (bottom) in model $ECS_{2xC} = 2.6$ K. Five different plant functional types are simulated: broadleaf trees (green), needleleaf trees (blue), C_3 grass (brown), C_4 grass (orange), and shrub (light green) in addition to bare soil (yellow).

References

1. R. Knutti, G. C. Hegerl, *Nat. Geosci.* **1**, 735 (2008).

2. J. G. Charney *et al.*, *Carbon Dioxide and Climate: A Scientific Assessment* (National Academy of Sciences, Washington, DC, 1979).

3. D. A. Stainforth *et al*., *Nature* **433**, 403 (2005).

4. G. H. Roe, M. B. Baker, *Science* **318**, 629 (2007).

5. D. L. Royer, R. A. Berner, J. Park, *Nature* **446**, 530 (2007).

6. IPCC, *Climate Change 2007: The Physical Science Basis. Contribution of Working Group I to the Fourth Assessment Report of the Intergovernmental Panel on Climate Change*. S. Solomon *et al.*, Eds., (Cambridge University Press, Cambridge, United Kingdom, New York, NY, USA, 2007), pp. 996.

7. R. Knutti, T. F. Stocker, F. Joos, G. K. Plattner, *Clim. Dyn.* **21**, 257 (2003).

8. C. E. Forest, P. H. Stone, A. P. Sokolov, *Tellus, Ser. A, Dyn. Meterol. Oceanogr.* **60**, 911 (2008).

9. N. G. Andronova, M. E. Schlesinger, *J. Geophys. Res. Atmos.* **106**, (D19), 22605 (2001).

10. J. M. Gregory, R. J. Stouffer, S. C. B. Raper, P. A. Stott, N. A. Rayner, *J. Clim.* **15**, 3117 (2002).

11. N. M. Mahowald *et al.*, *J. Geophys. Res. Atmos.* **111**, (D10), D10202 (2006).

12. MARGO Project Members, *Nat. Geosci.* **2**, 127 (2009).

13. P. Bartlein *et al*., *Clim. Dyn.* **37**, 775 (2011).

14. A. J. Weaver *et al*., *Atmos.-ocean* **39**, 361 (2001).

15. M. I. Budyko, *Tellus* **21**, 611 (1969).

16. V. Masson-Delmotte *et al*., *Clim. Dyn.* **26**, 513 (2006).

17. R. Bintanja, R. S. W. van de Wal, J. Oerlemans, *Clim. Dyn.* **24**, 197 (2005).

18. S. Manabe, M. J. Spelman, R. J. Stouffer, *J. Clim.* **5**, 105 (1992).

19. R. T. Sutton, B. W. Dong, J. M. Gregory, *Geophys. Res. Lett.* **34**, L02701 (2007).

20. J. D. Annan, J. C. Hargreaves, *Geophys. Res. Lett.* **33**, L06704 (2006).

21. J. Hansen *et al*., *The Open Atmospheric Science Journal* **2**, 217 (2008).

22. D. W. Lea, *J. Clim.* **17**, 2170 (2004).

23. T. Schneider von Deimling, H. Held, A. Ganopolski, S. Rahmstorf, *Clim. Dyn.* **27**, 149 (2006).

24. A. P. Ballantyne, M. Lavine, T. J. Crowley, J. Liu, P. B. Baker, *Geophys. Res. Lett.* **32**, L05712 (2005).

25. S. P. Harrison, K. E. Kohfeld, C. Roelandt, T. Claquin, *Earth Sci. Rev.* **54**, 43 (2001).

26. B. A. Maher *et al*., *Earth Sci. Rev.* **99**, 61 (2010).

27. M. Crucifix, *Geophys. Res. Lett.* **33**, L18701 (2006).

28. A. Schmittner, A. Oschlies, H. D. Matthews, E. D. Galbraith, *Global Biogeochem. Cycles* **22**, GB1013 (2008).

29. S. L. Thompson, S. G. Warren, *J. Atmos. Sci.* **39**, 2667 (1982).

30. W. R. Peltier, *Annu. Rev. Planet. Sci.* **32**, 111 (2004).

31. V. Ramaswamy *et al*., in *Climate Change 2001: The Scientific Basis. Contribution of Working Group I to the Third Assessment Report of the Intergovernmental Panel on Climate Change*, J. T. Houghton *et al.*, Eds. (Cambridge Univ. Press, Cambridge, UK, 2001), pp. 349–416.

32. EPICA Community Members, *Nature* **429**, 623 (2004).

33. J. Flückiger *et al*., *Science* **285**, 227 (1999).

34. N. M. Mahowald *et al*., *Geophys. Res. Lett.* **33**, L20705 (2006).

35. J. Hansen *et al*., in *Climate Processes and Climate Sensitivity*, J. E. Hansen, T. Takahashi, Eds. (American Geophysical Union, Washington, DC, 1984), vol. 29, pp. 130–163.

36. P. Köhler *et al*., *Quat. Sci. Rev.* **29**, 129 (2010).

37. K. E. Taylor *et al*., *J. Clim.* **20**, 2530 (2007).

38. A. J. Broccoli, *J. Clim.* **13**, 951 (2000).

39. C. D. Hewitt, J. F. B. Mitchell, *Clim. Dyn.* **13**, 821 (1997).

40. M. Yoshimori, T. Yokohata, A. Abe-Ouchi, *J. Clim.* **22**, 3374 (2009).

41. M. Yoshioka *et al*., *J. Clim.* **20**, 1445 (2007).

42. I. N. Sokolik, O. B. Toon, *J. Geophys. Res. Atmos.* **104**, (D8), 9423 (1999).

43. J. Perlwitz, I. Tegen, R. L. Miller, *J. Geophys. Res. Atmos.* **106**, (D16), 18167 (2001).

44. J. D. Shakun *et al*.; http://mgg.coas.oregonstate.edu/~andreas/data/schmittner11sci

45. J. Arbuszewski, P. deMenocal, A. Kaplan, E. C. Farmer, *Earth Planet. Sci. Lett.* **300**, 185 (2010).

46. E. Mathien-Blard, F. Bassinot, *Geochem. Geophys. Geosyst.* **10**, Q12011 (2009).

47. O. A. Saenko, A. Schmittner, A. J. Weaver, *J. Clim.* **17**, 2033 (2004).

48. W. B. Curry, D. W. Oppo, *Paleoceanography* **20**, PA1017 (2005).

49. J. R. Alder, S. W. Hostetler, D. Pollard, A. Schmittner, *Geosci. Model Dev.* **4**, 69 (2011).

50. M. Jun, M. L. Stein, *Technometrics* **49**, 468 (2007).

51. D. S. Oliver, *Math. Geol.* **35**, 681 (2003).

52. D. J. Frame *et al*., *Geophys. Res. Lett.* **32**, L09702 (2005).

53. J. D. Annan, J. C. Hargreaves, *Clim. Change* **104**, 423 (2011).

54. G. O. Roberts, J. S. Rosenthal, *J. Comput. Graph. Statist.* **18**, 349 (2009).

55. A. Schmittner, T. A. Silva, K. Fraedrich, E. Kirk, F. Lunkeit, *J. Clim.* **24**, 2814 (2011).

56. S. P. Harrison, I. C. Prentice, *Glob. Change Biol.* **9**, 983 (2003).

57. R. B. Alley, *Quat. Sci. Rev.* **19**, 213 (2000).

58. C. Waelbroeck *et al*., *Nature* **412**, 724 (2001).

59. V. L. Peck, I. R. Hall, R. Zahn, H. Elderfield, *Paleoceanography* **23**, PA3221 (2008).

60. K. Minoshima, H. Kawahata, K. Ikehara, *Palaeogeogr. Palaeoclimatol. Palaeoecol.* **254**, 430 (2007).

61. D. Isono *et al*., *Geology* **37**, 591 (2009).

62. F. Peterse *et al*., *Earth Planet. Sci. Lett.* **301**, 256 (2011).

63. K. Sawada, N. Handa, *Nature* **392**, 592 (1998).

64. A. E. Carlson *et al*., *Geology* **36**, 991 (2008).

65. I. S. Castañeda *et al*., *Paleoceanography* **25**, PA1208 (2010).

66. A. Ijiri *et al*., *Palaeogeogr. Palaeoclimatol. Palaeoecol.* **219**, 239 (2005).

67. M. Ziegler, D. Nurnberg, C. Karas, R. Tiedemann, L. J. Lourens, *Nat. Geosci.* **1**, 601 (2008).

68. H. W. Arz, J. Patzold, P. J. Muller, M. O. Moammar, *Paleoceanography* **18**, 1053 (2003).

69. B. P. Flower, D. W. Hastings, H. W. Hill, T. M. Quinn, *Geology* **32**, 597 (2004).

70. P. deMenocal, J. Ortiz, T. Guilderson, M. Sarnthein, *Science* **288**, 2198 (2000).

71. G. J. Wei, W. F. Deng, Y. Liu, X. H. Li, *Palaeogeogr. Palaeoclimatol. Palaeoecol.* **250**, 126 (2007).

72. C. Huguet, J. H. Kim, J. S. S. Damste, S. Schouten, *Paleoceanography* **21**, PA3003 (2006).

73. M. W. Schmidt, H. J. Spero, D. W. Lea, *Nature* **428**, 160 (2004).

74. G. Leduc *et al*., *Nature* **445**, 908 (2007).

75. H. M. Benway, A. C. Mix, B. A. Haley, G. P. Klinkhammer, *Paleoceanography* **21**, PA3008 (2006).

76. S. Steinke *et al*., *Quat. Sci. Rev.* **27**, 688 (2008).

77. S. Weldeab, D. W. Lea, R. R. Schneider, N. Andersen, *Science* **316**, 1303 (2007).

78. S. Weldeab, R. R. Schneider, M. Kolling, G. Wefer, *Geology* **33**, 981 (2005).

79. M. Kienast *et al*., *Nature* **443**, 846 (2006).

80. A. Koutavas, J. P. Sachs, *Paleoceanography* **23**, PA4205 (2008).

81. A. Jaeschke, C. Ruhlemann, H. Arz, G. Heil, G. Lohmann, *Paleoceanography* **22**, PA4206 (2007).

82. S. Weldeab, R. R. Schneider, M. Kolling, *Earth Planet. Sci. Lett.* **241**, 699 (2006).

83. L. Stott, A. Timmermann, R. Thunell, *Science* **318**, 435 (2007).

84. J. W. H. Weijers, E. Schefuss, S. Schouten, J. S. Sinninghe Damsté, *Science* **315**, 1701 (2007).

85. E. Schefuss, S. Schouten, R. R. Schneider, *Nature* **437**, 1003 (2005).

86. J. E. Tierney *et al*., *Science* **322**, 252 (2008).

87. C. Levi *et al*., *Geochem. Geophys. Geosyst.* **8**, Q05N12 (2007).

88. J. Xu, A. Holbourn, W. G. Kuhnt, Z. M. Jian, H. Kawamura, *Earth Planet. Sci. Lett.* **273**, 152 (2008).

89. E. C. Farmer, P. B. deMenocal, T. M. Marchitto, *Paleoceanography* **20**, PA2018 (2005).

90. J. Kaiser, F. Lamy, D. Hebbeln, *Paleoceanography* **20**, PA4009 (2005).

91. E. Calvo, C. Pelejero, P. De Deckker, G. A. Logan, *Geophys. Res. Lett.* **34**, L13707 (2007).

92. K. Pahnke, J. P. Sachs, *Paleoceanography* **21**, PA2003 (2006).

93. F. Lamy *et al*., *Earth Planet. Sci. Lett.* **259**, 400 (2007).

94. J. P. Sachs, R. F. Anderson, S. J. Lehman, *Science* **293**, 2077 (2001).

95. S. Barker *et al*., *Nature* **457**, 1097 (2009).

96. T. T. Barrows, S. J. Lehman, L. K. Fifield, P. De Deckker, *Science* **318**, 86 (2007).

97. B. Stenni *et al*., *Quat. Sci. Rev.* **29**, 146 (2010).

98. B. Lemieux-Dudon *et al*., *Quat. Sci. Rev.* **29**, 8 (2010).

99. K. Kawamura *et al*., *Nature* **448**, 912 (2007).

100. J. R. Petit *et al*., *Nature* **399**, 429 (1999).

101. E. Kalnay *et al*., *Bull. Am. Meteorol. Soc.* **77**, 437 (1996).

102. V. Ramanathan *et al*., *Science* **243**, 57 (1989).

103. Data are available for download at the National Climatic Data Center at NOAA www.ncdc.noaa.gov and at http://mgg.coas.oregonstate.edu/~andreas/data/schmittner11sci.